Journal of Volcanology and Geothermal Research 194 (2010) 75–99

Contents lists available at ScienceDirect

Journal of Volcanology and Geothermal Research

journal homepage: www.elsevier.com/locate/jvolgeores

The thermal signature of volcanic eruptions on Io and Earth

Ashley Gerard Davies [a,*], Laszlo P. Keszthelyi [b], Andrew J.L. Harris [c]

[a] Jet Propulsion Laboratory, California Institute of Technology. ms 183-501, 4800 Oak Grove Drive, Pasadena, CA 91109, USA
[b] USGS Astrogeology Branch, 2255 N. Gemini Drive, Flagstaff, AZ, USA
[c] Laboratoire Magmas et Volcans, OPGC, Université Blaise Pascal—CNRS, 5 Rue Kessler, 63038, Clermont-Ferrand, France

ARTICLE INFO

Article history:
Received 6 October 2009
Accepted 21 April 2010
Available online 16 May 2010

Keywords:
volcanism
Io
Earth
remote sensing
planetary science

ABSTRACT

We investigate a spectrum-based technique to identify the style of active volcanic eruptions on Jupiter's moon Io. Thermal remote sensing of Io has had to rely primarily on low-spatial-resolution data, similar to low-spatial-resolution satellite data applied to detecting and charting the temporal evolution of terrestrial hot spots. These terrestrial analyses use data from sensors designed to monitor the weather and sea surface temperature. On Io, such low-spatial-resolution data are used to classify eruption styles (modes of emplacement) by means of several criteria related to the temporal evolution of the infrared spectrum associated with the eruptive activity at each hot spot, which we term "thermal signature." We find that the ratio of the emission at 2 and 5 μm, and how this ratio changes with time, is often diagnostic of eruption style, even in low-spatial-resolution data. Tests using thermal data for terrestrial "ground truth" cases show that our classification system is valid on Earth. The results of our analysis can be used to aid in the design of future space-based instruments that can be used for volcano monitoring on Io, as well as Earth.

1. Introduction

Thermal remote sensing of terrestrial volcanic activity by spacecraft has relied on both high- and low-spatial-resolution data. High-spatial-resolution thermal data with pixel sizes of between 60 and 120 m are available from sensors such as *Landsat*'s Thematic Mapper (TM) and the *Terra* Advanced Spaceborne Thermal Emission and Reflection Radiometer (ASTER). These data have been used to extract and examine the thermal structure (the range and areal distribution of surface temperatures and resulting thermal emission spectrum) at active lava flows, domes and lakes (e.g., Carter et al., 2007; Davies et al., 2008a; Flynn et al., 1994; Oppenheimer et al., 1993b; Rothery et al., 1988; Vaughan et al., 2005). Although TM data have been used for thermal time-series analysis of persistent volcanic hot spots associated with lava dome extrusion (e.g., Glaze et al., 1989; Harris et al., 2003; Oppenheimer et al., 1993a), their temporal resolution (1 image every 16 days) is less than ideal for time-series analysis of transient volcanic phenomena which vary on time scales of a few hours. Thus, on Earth, data from weather satellites have been more commonly used for time-series analysis. These sensors include the Advanced Very High Resolution Radiometer (AVHRR) flown on the National Oceanic and Atmospheric Administration (NOAA) satellite series and the Imagers flown on the *Geostationary Operational Environmental Satellites* (*GOES*). The data are not ideal, with no short-wave infrared capability, low saturation levels (50 °C to 60 °C) and poor spatial resolution (1 to 4 km in the mid- and thermal infrared). However, the polar orbit of each NOAA platform allows one image of any terrestrial point to be acquired every 12 h and the geostationary orbit of *GOES* allows sampling every 15 to 30 min. Such data have been shown to be of value for generating high-temporal-resolution thermal time-series for hot spots associated with eruptive activity that waxes and wanes over time scales of minutes to days (e.g., Harris et al., 1997a,c; Wooster and Rothery, 1997b). An important advantage studying Earth as opposed to Io is that we usually know (albeit sometimes only in hindsight) the nature of the hot spot source, i.e., whether it is a lava fountain, lava lake, lava dome, or channel- or tube-fed flow. We can therefore assess and define the thermal output from a source of known character.

Here we investigate the possibility that eruption styles (mode of emplacement) on Jupiter's moon Io in future observations can be constrained using only low-spatial-resolution thermal data sets. Our work hinges on the notion that different styles of effusive activity have distinct "thermal signatures" that can be seen in temporal and spectral plots, even when the spatial resolution is poor. This concept is not new, with the "spectral feature space" method having been applied in a number of terrestrial cases (Dehn et al., 2002; Harris et al., 1995). Out of necessity, this type of analysis of hot spots has been well developed for remotely sensed data for active volcanism on Io. On Io, interpretations regarding the style of activity have been based on an analysis of the spatial, temporal and spectral character of the hot spot guided by Earth-based experiences. Table 1 describes the expected qualitative character of thermal signatures for a variety of eruption styles. The table consists of generalizations drawn from a host of observations of volcanic activity on Earth and Io. Because Table 1 is a

* Corresponding author. Tel.: +1 818 393 1775.
E-mail address: Ashley.Davies@jpl.nasa.gov (A.G. Davies).

0377-0273/$ – see front matter © 2010 Published by Elsevier B.V.
doi:10.1016/j.jvolgeores.2010.04.009

Table 1
Thermal signature and evolution of different eruption modes.

	Eruption type	Location	Thermal characteristics	Short-timeframe change	Long-timeframe change
	Lava fountains	Fixed	Intense short-wavelength thermal emission. Very high radiant flux densities. Highest color temperature.	Very short duration (~hours?)	Not seen unless event repeats: series of thermal spikes
	Lava lake	Fixed	Intense-to-moderate short-wavelength thermal emission. Variable radiant flux density. Variable color temperature.	Brief periods of overturning and enhanced thermal activity	Persistent hot spot
	Channelized flows	Wandering	Moderate short-wavelength thermal emission. Moderate radiant flux density. High color temperature down axis of channel.	Thermal source increases in size (lengthens) and undergoes surges	Flows eventually stop and cool
	Insulated and tube-fed flows ('a'a and pahoehoe flows)	Wandering, persistent thermal source	Low short-wavelength thermal emission. Low radiant flux density. Low color temperature.	Source increases in area and changes location	Location migrates, intensity varies, sometimes episodically. Peak thermal flux often away from vent but linked to vent by sinuous feature of extremely low thermal intensity (tube)
	Lava domes	Fixed. Gradual increase in size	Low short-wavelength thermal emission. Low radiant flux densities. Very low color temperature.	Small incandescent areas: occasional explosive activity to suddenly increase thermal emission and radiant flux density	Weeks-months-years. Not identified on Io
	Silicic lava flows	Gradual increase in size	Low-to-no short-wavelength thermal emission. Extremely low radiant flux densities. Extremely low color temperature.	Very stable	Years. Not identified on Io

Image credits: lava fountain: P. Mouginis-Mark. Lava lake: P. Vetsch. Open channel flow: US Nat. Park Service, S. Lopez. Pahoehoe flows: A. G. Davies. Lava dome: L. P. Keszthelyi. Silicic flow: A. J. L. Harris.

synthesis of observations, it would be disingenuous of us to suggest that these are predictions to be tested by observations. However, it is important to verify that these gross generalizations actually have some observational basis when applied to individual eruptions on Io and Earth.

In this paper, we compare the observations of Io to the general classifications given in Table 1. We then describe more quantitative methodologies that can be used to interpret thermal emission from Io. We then move on to comparisons with terrestrial examples to validate the classification methodology before making suggestions for future satellite missions for volcano monitoring on both Io and the Earth.

2. Io observations

Mafic/ultramafic volcanism on Io is driven by tidal heating as the body is distorted in its close elliptical orbit around the largest planet in our Solar System, Jupiter. Io's volcanic activity was discovered in 1979 by the *Voyager* mission (Morabito et al., 1979). While the lava composition was initially thought to be dominated by sulfur (e.g., Sagan, 1979), later Earth-based telescopic observations showed that silicate volcanism was present (Johnson et al., 1986; Veeder et al., 1994). It is estimated that ~500 km^3 of lava and other materials erupt onto the surface of Io every year (Blaney et al., 1995), as compared to ~4 km^3 for the Earth, including lava from mid-ocean ridges (e.g., Crisp, 1984; Simkin and Siebert, 1994). In the late 1990s, the *Galileo* mission showed that silicate volcanism was the dominant source of Io's infrared emissions (Davies et al., 2000, 1997; Lopes et al., 2001; McEwen et al., 1998a,b, 1997), though secondary sulfur lava flows and pyroclastics may be areally extensive (Williams et al., 2001b).

Observations of Io have been obtained from ground-based telescopes, instruments on the Earth-orbiting Hubble Space Telescope, and from spacecraft in orbit around Jupiter (*Galileo*) or during flybys (*Voyagers 1* and *2*, *Cassini*, and *New Horizons*). A comprehensive history and description of Io observations is provided in Davies (2007). Table 2 summarizes the spatial, spectral, and temporal resolutions of the different types of observations of thermal emission on Io achieved to date. Here we focus on thermal emission as seen by the *Galileo* Near Infrared Mapping Spectrometer (NIMS) and Earth-based telescopes, though key observations from other instruments will also be discussed.

One of the advantages of observing Io, as opposed to the Earth, is that Io has neither atmospheric absorption nor clouds to obscure the target. For example, surface imaging of the Earth is difficult between 5 and 8 μm due to absorption of the surface-emitted radiation by water vapour over much of this wavelength range. Io also has a greater temperature contrast between emplaced flows and background temperature (Io's surface temperature is 95–130 K; Earth's surface temperature is typically 300 K).

2.1. Galileo Near Infrared Mapping Spectrometer (NIMS)

From orbit around Jupiter, the *Galileo* spacecraft observed Io between June 1996 and mid-2002. It carried three main remote-sensing instruments, the Solid State Imaging experiment (SSI) camera, the Photo-Polarimeter Radiometer (PPR), and NIMS, which covered wavelengths from 0.7 to 5.2 μm (Table 2). NIMS could be operated in different modes, including a "hyperspectral" mode with 408 wavelengths and a "multi-spectral" mode during which data were collected at 17 wavelengths (Carlson et al., 1992). Satellite observations were generally obtained during the period of closest approach to Jupiter during *Galileo*'s elliptical orbit, which meant that batches of data were typically collected months apart. During the early part of the *Galileo* mission, the spacecraft remained far from the radiation belts around Io,

Table 2
Instrument characteristics for Io observations.

Spacecraft/facility	Instrument	Wavelength coverage (μm)	Number of bands	Typical spatial resolution (km pixel^{-1})	Highest resolution (km pixel^{-1})	Typical temporal resolution
Galileo	SSI	0.4–1.0	7	1–10	0.006–~1	Months
Galileo	NIMS	0.7–5.2	Up to 408	150–300	0.09–~1	Months
Galileo	PPR	0.4–1; 15–100[a]	2	250–300	15	Months
Cassini	ISS	0.258–1.002	21 WAC[b] 15 NAC[c]	~61	61	~Minutes during 1 flyby
Cassini	VIMS	0.3–5.1	315	>600	~600	1 flyby
New Horizons	LORRI[d]	0.4–0.9	1	~24	11	Minutes (1 flyby)
New Horizons	MVIC[d]	0.45–0.9	4	~75	45	Minutes (1 flyby)
New Horizons	LEISA[d]	1.25–2.5	λ/Δλ of 240–560	~180	137	Minutes (1 flyby)
Keck telescope	AO	1.12 to 4.67 (recent)	4	160	160	Minutes–hours
IRTF	IRCam	4.8–20	Up to 4	1800	1800	Hours
HST	WFPC2	UV, VIS	1–2	200	200	Months

Notes.
AO = Adaptive Optics.
HST = Hubble Space Telescope.
IRCam = InfraRed Camera (used with IRTF).
IRTF = Infrared Telescope Facility (on Mauna Kea, Hawai'i).
ISS = *Cassini* Imaging Sub-System.
NIMS = *Galileo* Near Infrared Mapping Spectrometer.
SSI = *Galileo* Solid State Imaging experiment.
VIMS = *Cassini* Visible-Infrared Mapping Spectrometer.
WFPC2 = Wide Field Planetary Camera 2 (on HST).
[a] The *Galileo* Photopolarimeter Radiometer (PPR) filter wheel did not behave with full functionality. The two usable filters were centred on 17 and 27 μm.
[b] *Cassini* Wide Angle Camera (WAC) has 25 filters; 21 are appropriate for studying volcanic thermal emission.
[c] *Cassini* Narrow Angle Camera (NAC) has 18 filters; 15 are appropriate for studying volcanic thermal emission.
[d] *New Horizons* imagers are the Long Range Reconnaissance Imager (LORRI); Linear Etalon Imaging Spectral Array (LEISA), a near-infrared spectral imager; and the Multispectral Visible Imaging Camera (MVIC).

providing spatial resolutions of hundreds of kilometres per pixel. High-spatial-resolution observations were made during later close flybys, yielding observations at spatial resolutions up to 0.5 km per pixel (Davies, 2003a; Lopes-Gautier et al., 1997, 1999; Lopes et al., 2001, 2004). NIMS was able to detect thermal emission down to a theoretical limit of around ~220 K (Smythe et al., 1995). A poor signal-to-noise ratio at the shortest detector wavelengths restricted the use of NIMS data at wavelengths shorter than ~1.5 μm.

Galileo confirmed the presence of over 150 individual active volcanoes, many with temperatures requiring active silicate volcanism (Davies, 2003b; Appendix 1 in Davies, 2007; Davies et al., 2001, 1997; Keszthelyi et al., 2001; McEwen et al., 1998a). The styles of eruption on Io generally had to be inferred from very-low-spatial-resolution data, with high-spatial-resolution observations by the SSI camera and NIMS being critical in testing these inferences at key eruptions. For example, data collected from the late *Galileo* flybys showed a probable lava lake at Pele (Radebaugh et al., 2004); insulated, pahoehoe-like flows at Prometheus and Amirani (Keszthelyi et al., 2001); open channel flows at Pillan (Williams et al., 2001a); and lava fountains at Pillan and in Tvashtar Paterae (Keszthelyi et al., 2001; Milazzo et al., 2005). The inferred styles of eruption on Io cover all the main types of mafic eruption on Earth, but often at spatial scales much larger than those witnessed terrestrially (e.g., Davies, 2007).

2.2. Earth-based observations

Earth-based telescopic observations have proven extremely valuable for long-term monitoring of Io's volcanism. For example, multi-wavelength infrared data provided the first definitive indications of active silicate (as opposed to sulfur) volcanism on Io (Johnson et al., 1988; Veeder et al., 1994). Despite their utility, these Earth-based data suffer from some important limitations in temporal, spatial, and spectral resolution (Table 2). The development of Adaptive Optics (AO), which removes much of the distortion caused by Earth's atmosphere, opened a new era in the observation of Solar System bodies, including Io (e.g., de Pater et al., 2004; Marchis et al., 2002, 2001). The spatial resolutions obtained (~160 km per pixel) are as good as many of the *Galileo* NIMS observations, and can easily resolve major hot spots on Io's surface (see Marchis et al., 2002). Currently, new AO observations obtain high-spectral-resolution data at wavelengths shorter than previously obtained with ground-based telescopes (e.g., Hom et al., 2007; Laver et al., 2007). Observations utilizing AO will probably be the best source of new Io data for at least the next decade.

2.3. Observations of lava fountains and channel-fed flows on Io

On Io, the absence of an atmosphere means that even a low gas content can produce lava fountains (Wilson and Head, 1981), so that high lava fountains may be more common on Io than on Earth (Davies, 1996). Still, lava fountains are the rarest eruption style observed on Io, partly because they are short-lived. For this reason, most observations come from ground-based telescopic measurements, which have a much longer baseline and higher temporal resolution than the *Galileo* mission. A noteworthy issue with observing lava fountains is that as the eruption continues, channel-fed lava flows can form around the fountains, mixing two different types of eruptive phenomena.

There is only one documented case where the thermal emission from a lava fountain was probably observed in isolation from lava flows. A telescopic observation in October 1996 detected a very short-lived thermal event right on the visible edge (limb) of Io (35° ± 15° W, 75° ± 15° N). Any associated lava flows would have been essentially invisible from the Earth (Stansberry et al., 1997). The 2- and 5-μm radiant fluxes were 723 GW μm^{-1} and 220 GW μm^{-1}, respectively. With a total thermal emission of 3.9×10^{12} W from an area of 13.7 km^2, the radiant flux density was 287 kW m^{-2}.

Other similar eruptions on Io have been classified as "outbursts," events that double Io's thermal emission at 4.8 μm (Blaney et al., 1995). Outbursts up to mid-2006 are listed in Spencer and Schneider (1996) and Davies (2007). The most powerful outburst witnessed on Io to date was at Surt (337.1° W, 44.9° N) on 22 February 2001 (Fig. 1) (Marchis et al., 2002). This eruption generated 7.8 ($\pm$0.6) $\times10^{13}$ W at its peak, almost the equivalent of the entire thermal emission from the rest of Io (10^{14} W: Veeder et al., 1994). No unusual thermal emission was seen two days before the event, and only a small anomaly was present one

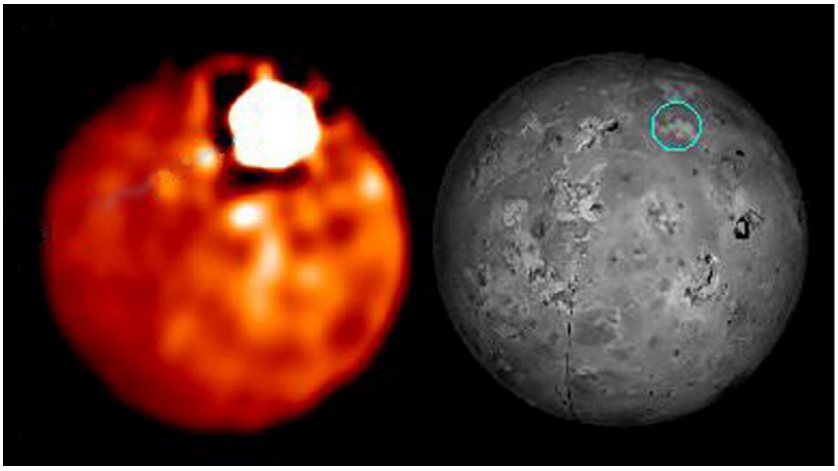

Fig. 1. The eruption of Surt in February 2001 (left), observed from Earth with the Keck telescopes on Mauna Kea, Hawai'i, using Adaptive Optics and the MISTRAL data processing algorithm (Marchis et al., 2002). The image on the right is a reference image. This is the most thermally powerful eruption ever observed on Io to date, being a rare type of "outburst eruption" during which the 4.8-μm spectral radiance output from the hot spot associated with the outburst exceeds that from the rest of Io.

day before the outburst. In this case the telescope was not available to monitor the waning of the eruption, so we cannot confirm that it was short-lived, only that it had a sudden onset. Peak 2- and 5-μm radiant fluxes were 16,500 GW μm^{-1} and 8100 GW μm^{-1}, respectively. The peak radiant flux density was 97 kW m^{-2} from an area of 804 km^2 (see Marchis et al., 2002; Davies, 2007). A similar outburst event was observed in January 1990 in the vicinity of Loki Patera (Veeder et al., 1994). This event is unique for the high temporal resolution of the data, as multiple wavelength observations were obtained over the course of 2 h. As the lava fountains died down during this period, the 2- and 5-μm radiant fluxes decreased from 3550 GW μm^{-1} and 1020 GW μm^{-1} to 910 GW μm^{-1} and 960 GW μm^{-1}, respectively (Davies, 1996). At its peak the eruption was emitting 1.1×10^4 GW from an area of 156 km^2, yielding a radiant flux density of 70.6 kW m^{-2}.

The interpretation that outbursts involve lava fountains (Davies, 1996) was confirmed by *Galileo*, which observed two active lava fountains: in Tvashtar Paterae in November 1999 and Pillan in May and possibly June 1997. In the case of Tvashtar, near-simultaneous Earth-based telescopic observations gave the first indication that a major eruption was underway. While the NIMS data were too badly saturated to extract useful thermal data, the spatial distribution of thermal emission could be approximately reconstructed from the February 2000 SSI camera images (Fig. 2). The resulting picture showed a 25-km-long fissure with incandescent fountains reaching ~1 km in height (Keszthelyi et al., 2001; Milazzo et al., 2005). Tvashtar was observed in eruption again in 2001 (Marchis et al., 2002), emitting over 10 TW, and again in 2007 by the *New Horizons* spacecraft (Spencer et al., 2007). The 1997 Pillan eruption was described by McEwen et al. (1998b), Davies et al.

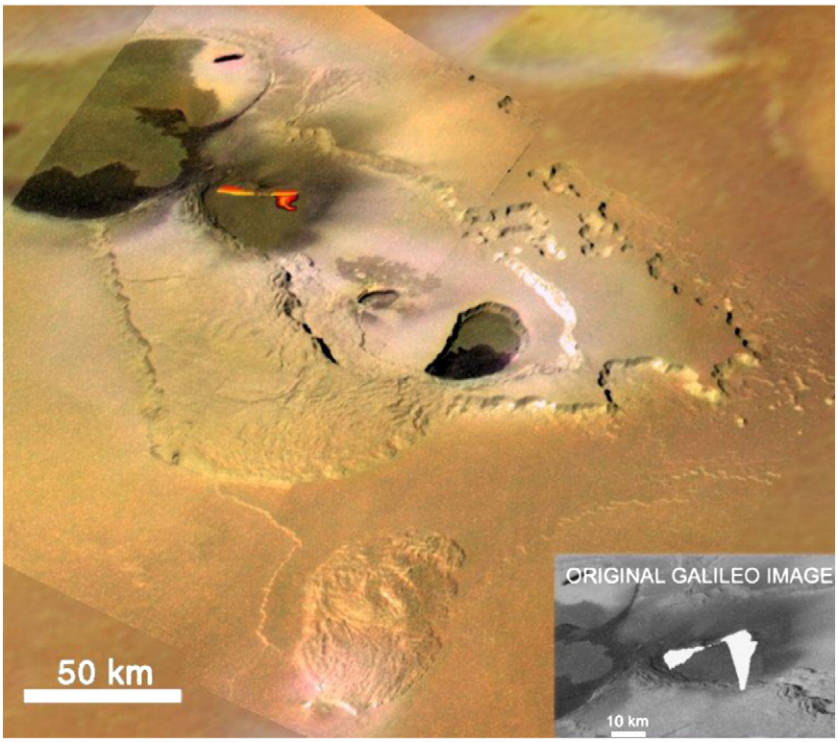

Fig. 2. Tvashtar Paterae, Io. In November 1999 the *Galileo* Solid State Imaging experiment (SSI) observed large lava fountains erupting from a 25-km-long fissure (inset image) (Keszthelyi et al., 2001). The intensity of the thermal emission caused detector bleeding down the image. The color image includes a reconstruction of the lava fountains and associated flows, also from Keszthelyi et al. (2001). Image credit: NASA PIA02545.

(2001), Williams et al. (2001a) and Keszthelyi et al. (2001). This eruption produced a 400-km-diameter (dark and circular) pyroclastic deposit and 8- to 11-m-thick sheet flows that covered over 3000 km^2 in less than five months. During the outburst, and in subsequent activity, >56 km^3 of lava was erupted (Davies et al., 2007) that covered over 5600 km^2 in less than a year (Williams et al., 2001a). Peak effusion rates probably exceeded 10^4 m^3 s^{-1} (Davies et al., 2007).

NIMS obtained a sequence of Pillan observations that caught the eruption close to its onset in May 1997 and at its height in June 1997, when the thermal signature was that of a likely lava fountain and associated lava flows (Fig. 3). Over the next two years NIMS observed the subsequent cooling of the emplaced flows (Davies et al., 2001), with the wavelength of peak emission gradually shifting to longer wavelengths. At the same time, the total thermal emission decreased, consistent with lower surface temperatures. The trend reversed in May 1999, when there was a renewal of activity in the Pillan region (Davies et al., 2001), yielding a slight increase in short-wave infrared thermal emission.

Currently, there is no reliable method to separate the thermal emission from lava fountains and their associated channel-fed flows on Io. In a sense this not a problem because the two eruption styles are expected to be closely associated with each other. The significance of isolating lava fountains from their associated flows is discussed in the conclusions.

2.4. Observations of lava lakes on Io

Two examples of probable active lava lakes on Io are found in Loki Patera and at Pele. Io's long-term volcanic thermal emission is dominated by Loki Patera, which has an average output of $\approx 10^{13}$ W, or 10% of Io's total thermal emission. This percentage often increases to more than 15%, and can also drop to less than 6% (Matson et al., 2006). Temperatures >990 K (too hot for sulfur) have been derived from NIMS data obtained in June 1997 (Davies, 2003a). At the same time, SSI also detected surfaces in excess of 700 K at Loki Patera in an eclipse observation (Davies, 2003a; Matson et al., 2006). In NIMS data obtained between 1997 and 1999, Loki Patera exhibited a low radiant flux density of 0.09 to 0.62 kW m^{-2} (see Matson et al., 2006).

Loki Patera undergoes infrared brightenings that for many years were periodic (Rathbun et al., 2002). Rathbun et al. suggested that this periodicity was caused by the foundering of a thick crust on a lava lake. This hypothesis is supported by the lake-like appearance of Loki Patera, the observed temperature distribution in high-resolution (3–5 km per pixel) NIMS data (Davies, 2003a), the evolution of the thermal emission spectrum over time (Fig. 4) (Matson et al., 2006), and the fact that the Loki Patera surface exhibits specular reflectance (Turtle et al., 2004), suggesting a relatively smooth and glassy surface. Loki Patera appears to contain a massive lava lake with a surface area of $\approx 2.15 \times 10^4$ km^2.

In contrast to Loki Patera, Pele has been a more consistent thermal source (Fig. 5). A sequence of NIMS observations showed that Pele had a persistent thermal emission spectrum peaking at a wavelength around 2.5 μm, and steady thermal emission (~230 GW) from six NIMS observations from 1996 to 1999 (Davies et al., 2001). Similar thermal emission was observed by the *Voyager* InfraRed Imaging Spectrometer (IRIS) (Carr, 1986; Pearl and Sinton, 1982) and by ground-based telescopes utilizing adaptive optics (de Pater et al., 2004; Marchis et al., 2002, 2005). Effusion rate estimates of ~250 to ~340 m^3 s^{-1} (Davies et al., 2001) showed that effusion rates during the *Galileo* epoch were similar to the effusion rate derived from *Voyager* data (~350 m^3 s^{-1} [Carr, 1986]). The style of activity at Pele, as inferred from low-spatial-resolution NIMS data, suggests that the surface is being constantly renewed without growth of the area covered by lava. The lava is somehow laterally confined, suggesting that Pele is most probably a large, active, overturning, pit-confined lava lake (Davies et al., 2001). High-spatial-resolution SSI observations showed that the margin and center of the lake are being constantly disrupted (McEwen et al., 2000; Radebaugh et al., 2004). To date, Pele is the only volcano on Io to exhibit such a consistent

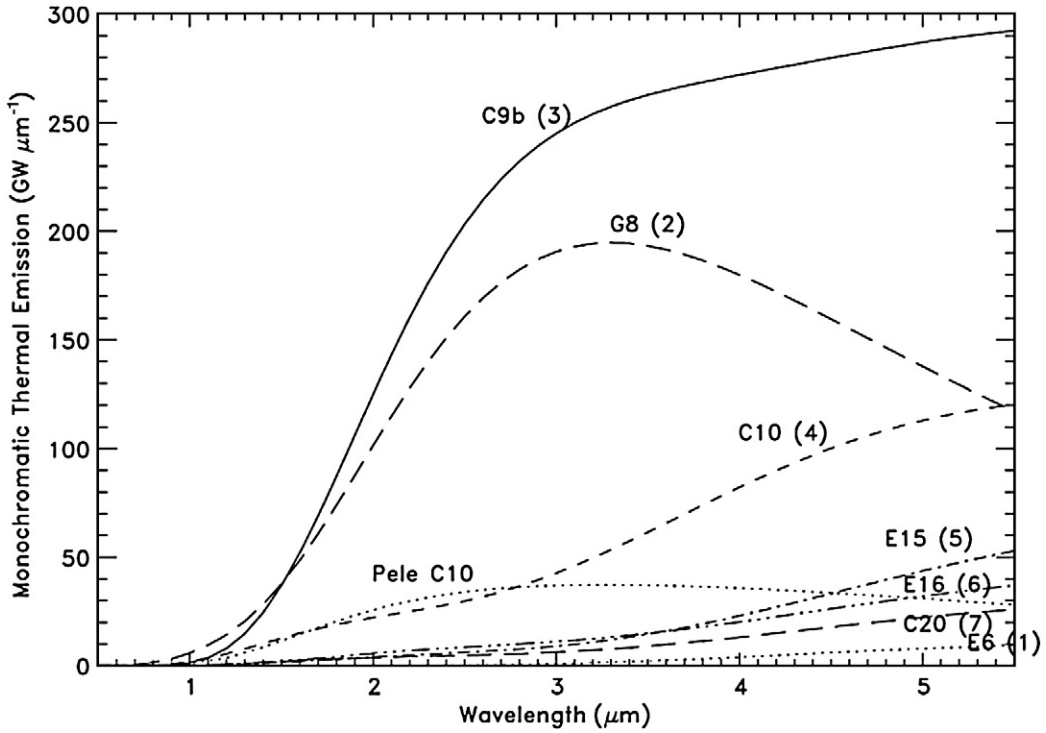

Fig. 3. The evolution of thermal emission from Pillan, on Io, as seen by the *Galileo* Near Infrared Mapping Spectrometer (NIMS) between 20 February 1997 (orbit E6) and 5 May 1999 (orbit C20). The numbers in parentheses indicate the order in which the data were acquired. Thermal emission reached a peak in June 1997 (orbit C9) during an "outburst" eruption. This spectrum and subsequent evolution is characteristic of lava fountains feeding channel-fed flow fields (Davies et al., 2001). The decrease in thermal emission is characteristic of cooling lava flows in an ionian environment. For comparison, the thermal emission spectrum from Pele is also shown. The letter–number combinations refer to the *Galileo* orbit around Jupiter (see Davies, 2007).

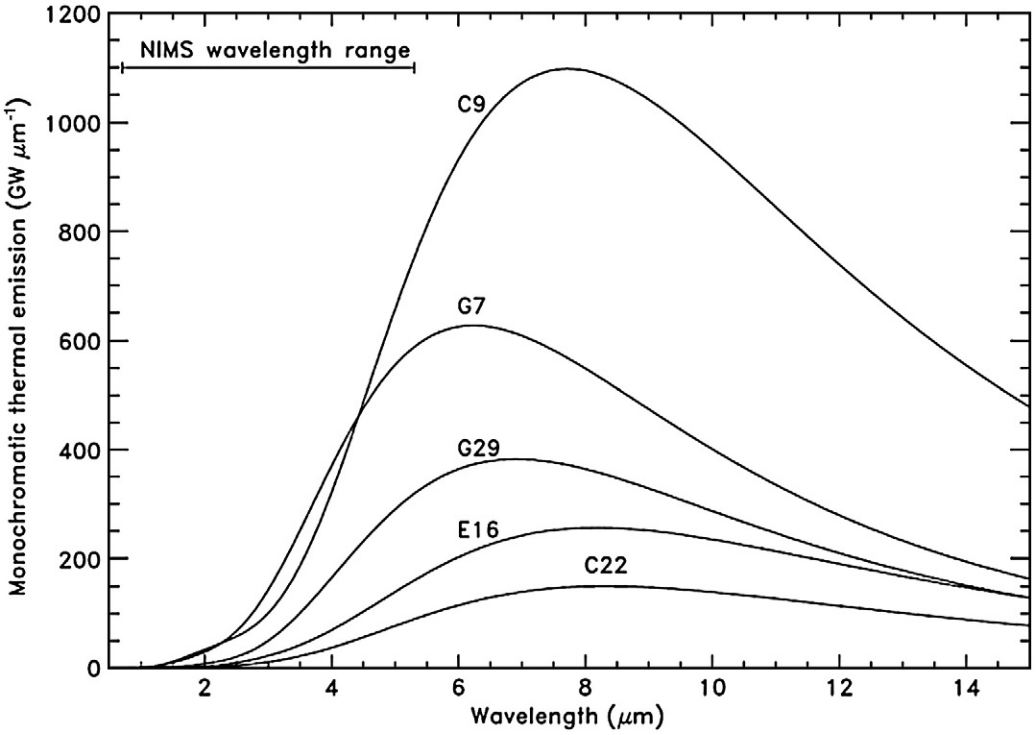

Fig. 4. The evolving thermal emission from Loki Patera as derived from low-spatial-resolution *Galileo* Near Infrared Mapping Spectrometer data (Matson et al., 2006) obtained on 5 April 1997 (*Galileo* orbit G7), 25 July 1997 (orbit C9), 21 July 1998 (orbit E16), 14 August 1999 (orbit C22) and 28 December 1999 (orbit G29). The appearance of Loki Patera, the periodic variability of 3.5-μm and 3.8-μm thermal emission over a number of years (Rathbun et al., 2002), and the observed temperature distribution in high-resolution NIMS data (Davies, 2003a; Matson et al., 2006), suggest Loki Patera may be a massive lava lake. Figure © A. G. Davies (2007).

thermal signature. The persistence of the metastable red pyroclastic deposit around Pele is another indication that this eruption has been constant. Analysis of NIMS data obtained on 20 July 1998 yielded a total thermal emission of 280 GW, 2- and 5-μm radiant fluxes of 39 and 33 GW μm^{-1}, and a radiant flux density of 17 kW m^{-2}. The latter two numbers are similar to those of active lava lakes on Earth.

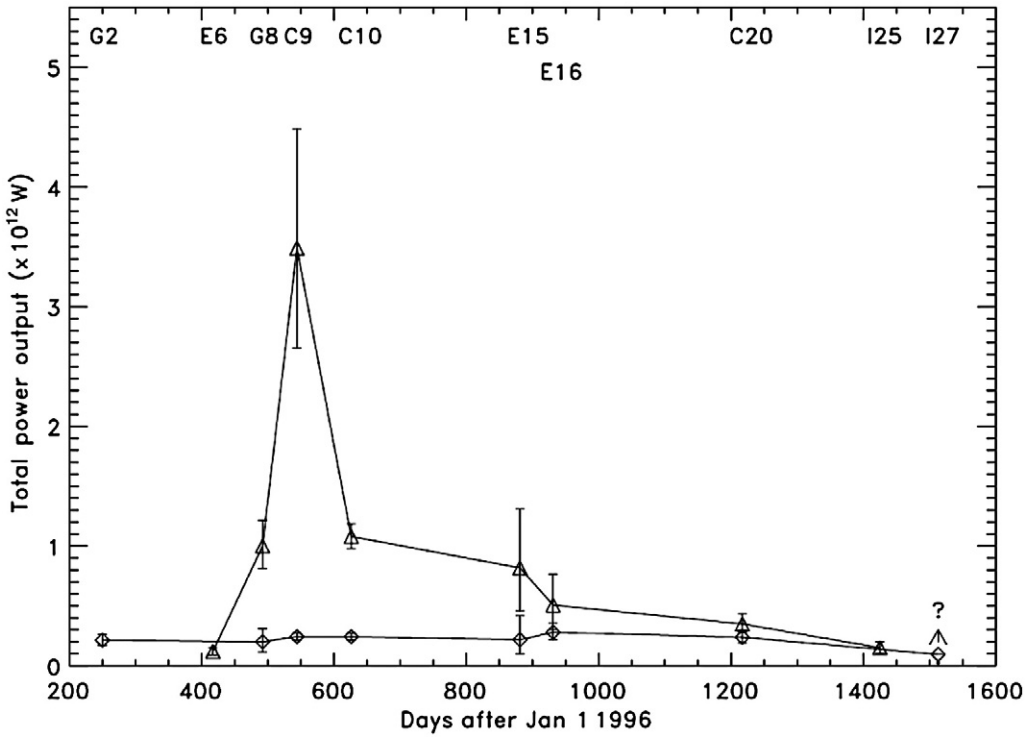

Fig. 5. The variability of total thermal emission from Pele (diamonds) and Pillan (triangles). The datum at I27 marked with a "?" is a minimum value for Pillan. Pele's thermal emission is very steady, and does not appear to have changed significantly since first observed in 1979 by *Voyager*. Pillan's thermal emission rose to a peak in June 1997 and then declined over the next few years as the emplaced lava flows cooled. From Davies et al. (2001).

Other volcanoes on Io (Janus Patera, Isum and Tupan Patera) have occasionally exhibited thermal emission characteristic of lava lakes, although the very low temporal resolution of observations makes tracking of activity (and a definitive classification of activity) difficult. Only rarely observed by *Galileo* NIMS, Janus Patera was observed using AO in 2001 (Marchis et al., 2005). Janus had a total thermal emission of 53 GW from an area of 4.29 km^2 and a radiant flux density of 12.3 kW m^{-2}. A day later, the area had increased to 10 km^2, thermal emission was 300 GW, and the radiant flux density had dropped to 8 kW m^{-2}. It is unknown whether this activity was caused by overturning of a lava lake crust, or by the emplacement of new flows.

At about the same time (December 2001), Isum was emitting 47 GW from an intense hot spot (>800 K) with an area of only 1.2 km^2 (Marchis et al., 2005), yielding a radiant flux density of 40.3 kW m^{-2}. It is likely that this eruption was either a rapidly overturning lava lake or small lava fountains to produce such a large thermal emission from a relatively small area.

In NIMS data, Tupan Patera has a thermal emission spectrum consistent with either a quiescent lava lake or cooling flows (Ennis and Davies, 2005). However, an AO observation in 2001 showed Tupan Patera emitting 480 GW from an area of 44 km^2 (Marchis et al., 2005), yielding a radiant flux density of 11 kW m^{-2}. The radiant flux density from Tupan Patera at this time was considerably more than the average of 2.73 kW m^{-2} derived from NIMS data, and was comparable to the radiant flux density at the Pele lava lake. From both NIMS and AO data, Tupan Patera is a good candidate for an active lava lake, although data are not conclusive.

2.5. Observations of insulated flow fields on Io

Because insulated lava flow fields, by definition, have thick, stable crusts that take considerable time to form, they are necessarily long-lived. Numerous examples have been seen on Io, with those at Amirani and Prometheus being the two best-studied examples. Amirani has the largest active lava flow field known in the Solar System. The flow field is 300 km-long and about 80 km wide. Comparison of images with a spatial resolution of 200 m per pixel acquired in October 1999 and November 2000 showed the presence of 23 new lobes covering a total of 620 km^2, suggesting an eruption rate of ~500 $m^3\ s^{-1}$ (Keszthelyi et al., 2001). Comparison with data from the 1979 *Voyager* flybys suggests that Amirani may have been continually active for over 20 years, but with the focus of activity shifting around within the flow field (McEwen et al., 1998a).

In the case of Prometheus, a lava flow field of some 3400 km^2 (Veeder et al., 2009) was emplaced in the 16 years between *Voyager* and the first *Galileo* observations. The active plume seen by *Voyager* in 1979 apparently persisted over those 16 years, with its characteristic annular plume deposit, rich in SO_2, migrating westwards some 80 km, keeping pace with the advancing flows. High-spatial-resolution SSI data revealed the emplacement of small individual lava flows, mostly on top of older lava flows (Keszthelyi et al., 2001), in a manner strongly reminiscent of Hawaiian pahoehoe flow fields (Davies, 2007; Davies et al., 2006b).

Prometheus (Fig. 6) is a good example of numerous ionian hot spots interpreted to be tube-fed, pahoehoe lava flows. NIMS spectra show an increase in emission towards longer wavelengths, indicating a large area at relatively low temperatures (Davies et al., 2000, 1997). Although the total thermal emission from these sites varies with time, the shape of the thermal emission spectrum does not change significantly. This is an indication that the style of eruption, and consequently the spectral thermal emission signature, stays the same, but occurs over varying areas (Davies, 2003b; Davies et al., 2006b; Ennis and Davies, 2005). In low-resolution data it is difficult to tell the difference between cooling lava flows and cooling lava lake crust, although longer-term behaviour (i.e., movement of the hot spot by tens of kilometers) should differentiate flows from lakes (Davies et al., 2005), as does radiant flux density. At Prometheus and Amirani, high-resolution SSI and NIMS data showed individual, recently emplaced flow fields, almost certainly fed by lava tubes (Keszthelyi et al., 2001; Leone et al., 2009). An actively overturning lava lake has a higher radiant flux density than pahoehoe flows. Similarly shaped spectra are seen at multiple locations on Io, including from newly emplaced flows at Zamama, and from activity within Tupan and Gish Bar Paterae (Davies, 2003b).

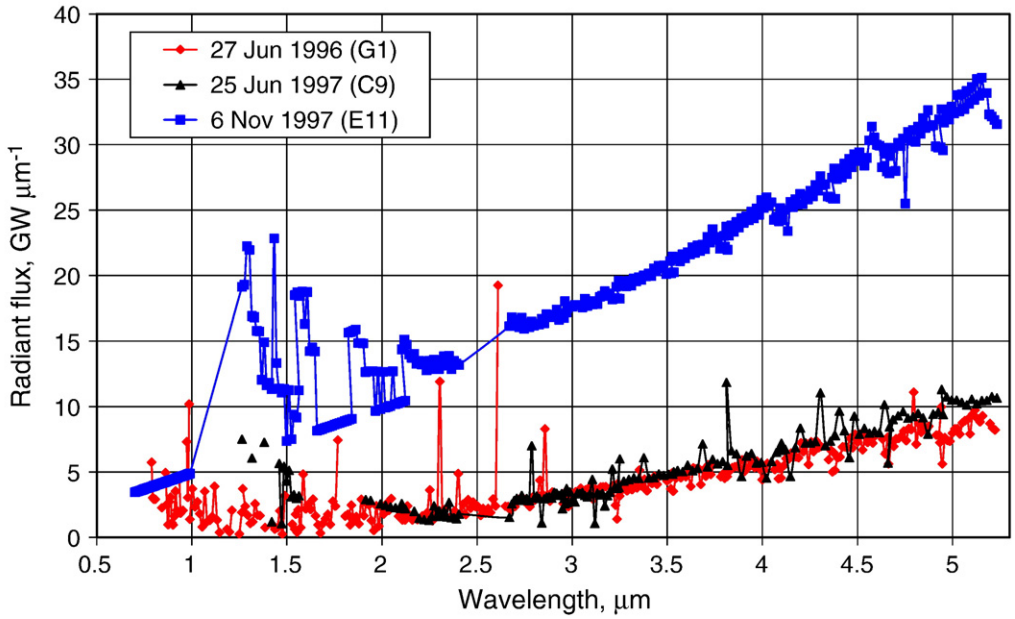

Fig. 6. Raw *Galileo* NIMS spectra of Prometheus, obtained in darkness. The three observations used are G1INHRSPEC01 (Orbit G1, 27 June 1996); C9INCHEMIS04 (Orbit C9, 25 June 1997); and 11INHRSPEC01 (Orbit E11, 6 November 1997). The ratio of thermal emission at two wavelengths does not greatly change, even when intensity greatly varies. The spikes in the data are removed during data reduction. All null values have been removed. The full spectra are broken down into individual grating position spectra (up to 24) before fitting with models to derive temperature and areas (see Davies, 2007, Chapter 3; Davies et al., 2000).

2.6. Observations of other types of volcanic centers on Io

The eruptions described above are the best examples of each style of effusive eruption witnessed on Io. There are also many examples of more ambiguous eruptions on Io. These tend to be small or cool hot spots with most of the thermal emission at longer wavelengths. They could be produced by (a) cooling lava of a now inactive flow field, (b) sulfur-rich volcanism, or (c) some mix of these. We discount the possibility that these sources are examples of low-temperature silicate volcanism analogous to terrestrial lava domes and silicic (high silica content) lava flows because nothing has yet been seen on Io that looks morphologically like a silicic flow. Every indication is that Io's dominant lavas are erupted at high temperatures and have low viscosities.

3. Quantitative analysis of the Io observations

Given that Table 1 was partially derived from the Io experience, it is no surprise that there is a good qualitative match to, firstly, the characteristics

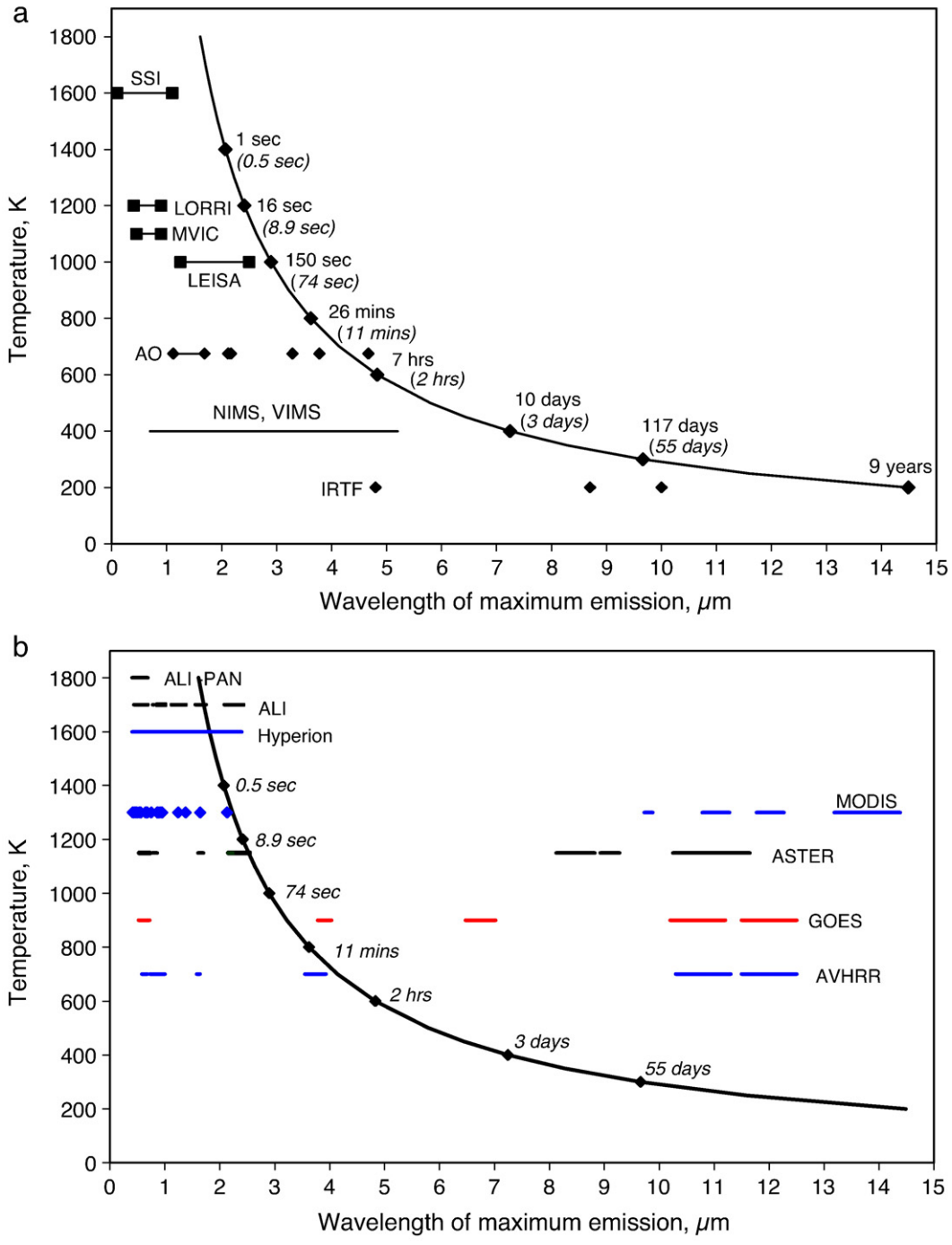

Fig. 7. a). Variation in wavelength of peak thermal emission with temperature (as determined using Wien's Law), with the wavelength ranges of different imagers that have observed Io. The curve is annotated with cooling times for newly emplaced basalt on the surface of Io and, in brackets, for a similar basalt flow on Earth. These data were produced using the model described in Davies (1996): see also Davies (2007). Atmospheric interactions lead to faster cooling on Earth than on Io. Although thermal emission from young surfaces (with ages <15 h on Io) peak in the NIMS wavelength range, NIMS is ideal for studying thermal emission from surfaces with ages from days to months as it is capable of detecting pixel brightness temperatures down to ≈200 K (Smythe et al., 1995). b). Variation in wavelength of peak thermal emission with temperature for the terrestrial case, showing wavelength ranges of various terrestrial satellite-based imagers.

of the hot spots outlined in the Table 1 classification, and secondly, to the observations associated with each activity style outlined above. However, additional insights can be obtained via a more quantitative examination of the NIMS data. In particular, we are interested in determining the least data from which eruption style can be determined. For example, the high spectral resolution achieved by NIMS across a wide wavelength range (0.7 to 5.2 μm) is not replicated in current terrestrial data due to the presence of regions of atmospheric opacity within this waveband. Nor is such a wide wavelength likely for Io observations in the near future. Therefore it is important to consider the best wavelength selection for classifying eruption style, and thus constrain the physical processes taking place.

To begin this analysis, it is useful to consider some basic aspects of thermal emission. If a lava body were emplaced and allowed to cool to ambient temperature, there is a progressive and predictable shift in the wavelength of peak thermal emission to longer wavelengths (described using Wien's Law) that can be used to infer the age of the surface since initial exposure. The temperature and wavelength of peak thermal emission relationship is shown in Fig. 7. Over-plotted on the curve in Fig. 7a are the cooling times for a thick basaltic lava flow emplaced on the surfaces of Io and Earth (Davies, 1996). Any process that serves to increase the area of the lava within a pixel, or change the average age of the lava within the pixel (e.g., an increase in the amount of young lava in a pixel as a result of an increase in effusion rate or because of crust overturn in a lava lake) will adjust this relationship. This adjustment is exacerbated by the fact that fresh lava at high temperatures contributes disproportionally large amounts of radiance at shorter wavelengths, and much less at longer wavelengths. The temporal variation in peak emission wavelength is therefore a time-integrated "age" of the lava within the pixel, heavily modulated by processes that serve to expose high-temperature material to the sensor.

We now describe how monitoring the change in the position of peak emission of the volcano's integrated thermal emission spectrum, as a function of time, is a powerful indicator of style of eruption. In order to achieve this eruption style characterization, it is important to obtain data on both sides of the peak of thermal emission. In principle, because the shape of the thermal emission spectrum is well-known, only one measurement on each side of the peak is required to broadly localize the peak.

In order to reliably bracket the peak of thermal emission for active lava at ~1500 K (a typical eruption temperature for basalt), the optimal short-wavelength should be ≤2 μm, which corresponds to a cooling time of ~1 s. In the case of ultramafic or superheated lavas seen at the vent, it is desirable to go to even shorter wavelengths (~0.6 μm to 1 μm), especially if the goal is to pin down the very highest temperatures on the volcano. However, if the goal is to constrain the eruption style with low-spatial-resolution data, these very short wavelengths are of less value because the bulk of thermal emission is at longer wavelengths. For well-insulated lava, the radiant flux at ~1 μm will be much less than at 2 μm, and thus much harder to measure.

Examining Fig. 7 shows that additional bands at approximately 3, 5, 8 and 12 μm would allow the peak of thermal emission to be tracked as the lava surface ages from seconds to weeks. Atmospheric windows exist near these wavelengths, specifically between 3 and 4 μm, close to 5 μm, and between 9 and 12 μm. Thus it is possible to use these bands for monitoring Io's volcanism from the surface of the Earth or for observing volcanism on Earth from space. However, if one did not have access to all five of these waveband regions, which wavelengths would provide the most information? We suggest that measurements at 2 and 5 μm provide a good compromise. NIMS data, with good spectral resolution between 2 and 5 μm, can be used to test our suggestion that a metric as simple as the ratio of thermal emission measured at 2 and 5 μm is useful for understanding the style of eruption at a volcano.

The appropriateness of this wavelength selection can be demonstrated quantitatively by examining thermal emission spectra by eruption style. In Figs. 8 and 9, the ratio of thermal emission at 2 μm to thermal emission at any other wavelengths between 2 and 12 μm (2:*x*) is given for what has been inferred to be tube-fed pahoehoe flows (Fig. 8a), lava lakes (Fig. 8b), and a lava fountain feeding channel-contained lava (Fig. 9). In the case of pahoehoe flows, the lowest ratio (the greatest difference in thermal emission at the two wavelengths) is obtained at 6.5 μm, with little change in the 2:*x* ratio between 5.5 μm and 7 μm. In the case of the fountain-fed lava flows, the smallest 2:*x* ratios occur between 3.5 and 7.5 μm. Thus, 5 μm is an appropriate wavelength to use with 2 μm to discriminate between cases, with 2:5-μm ratios being low (<0.3) for tube-fed pahoehoe flows, to a constant 0.5 to 1 for active lava lakes, and, in this example, about 0.5 for fountains and channel-fed flows, a ratio that decreases to 0.1 or less with time.

Fig. 10 shows the plot of 2- and 5-μm radiant fluxes for a number of ionian volcanoes. The major styles of eruption discussed in Section 2 can be identified on this plot. For example, the 2001 Surt lava fountains had a 2:5-μm ratio just over 2. At Pillan, as the fountains died out and the lava surfaces became cooler, the ratios declined with time. The postulated active lava lake with low fountains at Pele has a 2-μm radiant flux that roughly matches the 5-μm radiant flux, so that the 2:5-μm emission is very close to one (1.1 in July 1998).

In contrast, the insulated (tube-fed pahoehoe) flows at Prometheus, Amirani and Zamama have thermal emission spectra dominated by relatively cool crusts in the 350 K to 450 K range, so that the 5-μm radiant flux is much greater than at 2 μm. Now, the 2:5-μm ratio declines to less than one. Because long-lived tube-fed lava flow activity and quiescent lava lakes are the most common style of volcanism on Io, it is no surprise that many ionian volcanoes exhibit this spectral signature.

We note that it is not possible to differentiate between the cooling crust on a stagnant (quiescent) lava lake and insulated (tube-fed) flows from the 2:5-μm emission ratio alone. Gish Bar Patera and Tupan Patera are good examples of locations where we are unable to confidently determine whether the patera floors are being covered by insulated (tube-fed, inflating pahoehoe) lava flows or contain a quiescent, well-crusted, lava lake. However, with a longer time-series and even moderate spatial resolution, it may be possible to distinguish these eruption styles. For example, cyclic changes in radiance may be expected at an overturning lava lake, and hot spots will migrate if the lava flow extends into new territory.

In summary, the ratio of emission between 2 and 5 μm can be used to distinguish major classes of eruption (i.e., lava fountains and open flows versus insulated lava flows and quiescent lava lakes). This classification builds on an established basis of other two-band-spectra-based classifications, whereby relatively cool features (domes, and well-insulated or tube-fed flows) will have similar emissive characteristics at 3 to 5 μm and at 10 to 12 μm, but higher temperature features (lava fountains and open channels) will exhibit stronger emission at shorter wavelengths (e.g., Carn and Oppenheimer, 2000; Davies, 1996; Dehn et al., 2002; Flynn and Mouginis-Mark, 1995; Harris et al., 1997b). Models of thermal emission from different eruption styles reproduce these results (Davies, 1996). In our case, the 2:5-μm emission ratio considers the age of the surface crust, where the younger the crust, the greater the emission at 2 μm, and hence the higher the ratio. The ratio is also insensitive to the spatial scale of the activity (both the 2 and 5-μm radiant fluxes would increase and decrease proportionally with the area covered by the feature). Thus the 2:5-μm emission ratio is an effective method to separate the style of an active eruption from its areal extent, especially for persistent eruptions. However, additional information is needed to differentiate within these two (hot and insulated) end members. Furthermore, the 2:5-μm emission ratio works only for active lavas. Other (longer) wavelengths are more appropriate for studying the products of eruptions that have ceased, even recently. At that point, the ratio becomes much less than 1, with emission at 2 μm being vanishingly small, and all we can deduce is that we have an inactive and cooling surface.

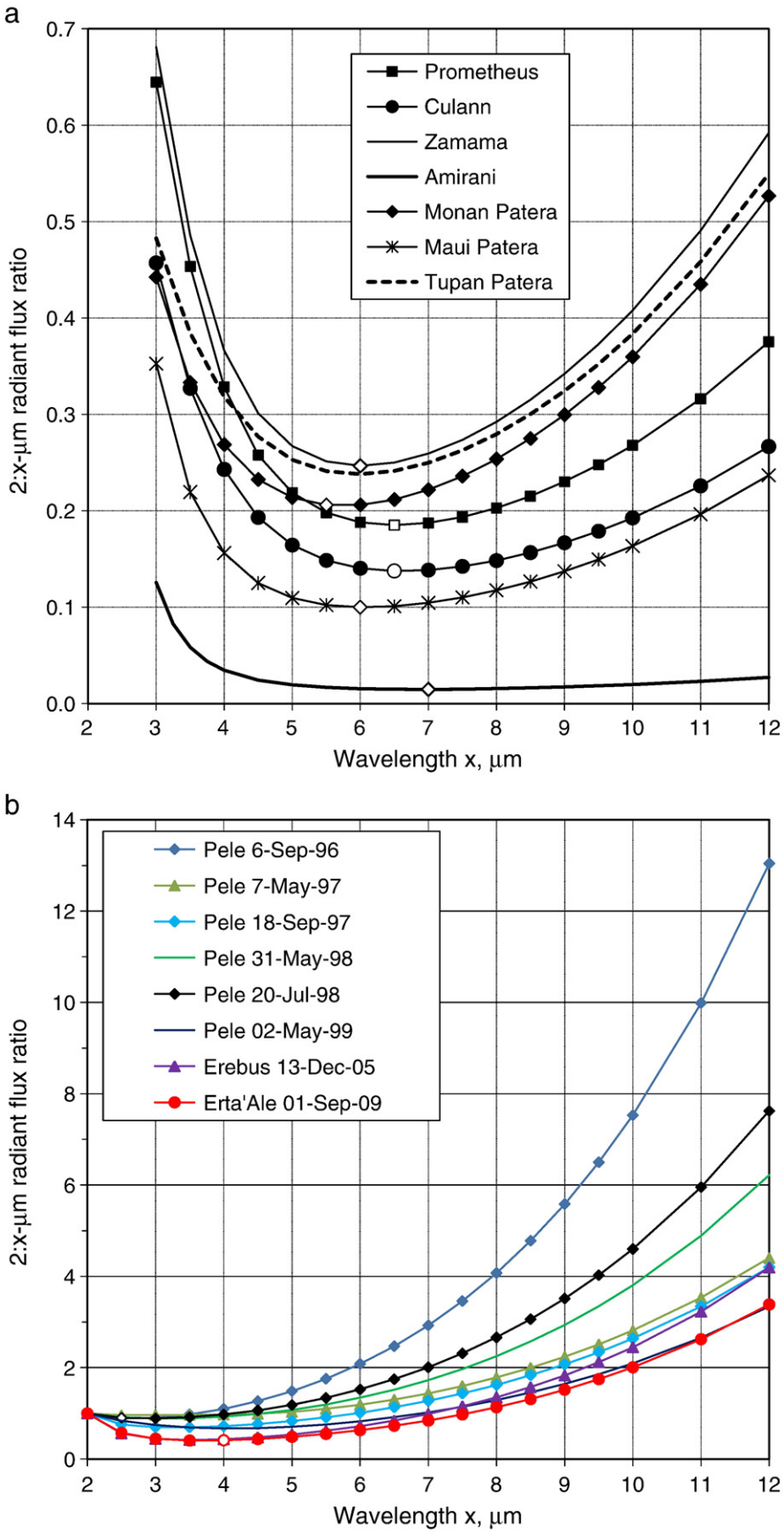
a
Prometheus
Culann
Zamama
Amirani
Monan Patera
Maui Patera
Tupan Patera
2:x-µm radiant flux ratio
Wavelength x, µm
b
Pele 6-Sep-96
Pele 7-May-97
Pele 18-Sep-97
Pele 31-May-98
Pele 20-Jul-98
Pele 02-May-99
Erebus 13-Dec-05
Erta'Ale 01-Sep-09
2:x-µm radiant flux ratio
Wavelength x, µm

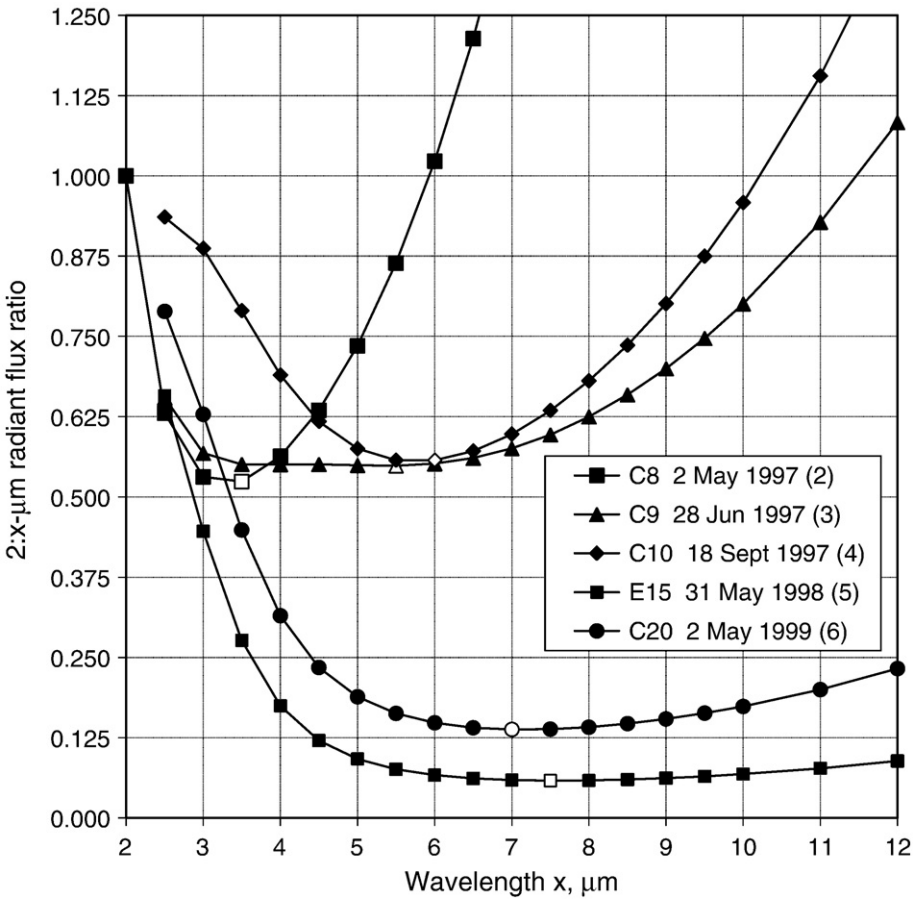

Fig. 9. The ratio of the 2-µm radiant flux to the radiant flux at all other wavelengths between 2 and 12 µm (*x* µm) for the Pillan eruption that peaked in June 1997, including a bright precursor in May 1997. Hollow data points indicate minimum values of the 2:*x*-µm thermal emission ratio (the greatest difference in thermal emission at the two wavelengths).

4. Comparison with terrestrial data

Similar techniques for identifying and classifying active volcanic phenomena on the Earth have been tested using time-series data from satellite-based sensors for lava fountains, lava flows, lava lakes, domes and insulated flows. For example, the temporal variation in satellite-derived heat (and mass) flux has been defined for fountain-fed flows (e.g., Harris and Neri, 2002), pressurized and persistent effusive lava eruptions (e.g., Harris et al., 2000a), lava lakes (e.g., Wright and Pilger, 2008), lava domes (e.g., Oppenheimer et al., 1993a), and highly insulated silicic lava flows (e.g., Harris et al., 2003). Descriptions of the spatial distribution of radiant flux density apparent in satellite-based data are also available for fountain-fed flows (e.g., Harris et al., 1995), channel-fed flows (e.g., Wright et al., 2001), tube-fed pahoehoe (e.g., Flynn et al., 1994), 'a'a flows (e.g., Oppenheimer, 1991), lava lakes (e.g., Davies et al., 2008a; Harris et al., 1999b), lava domes (e.g., Oppenheimer et al., 1993a), and silicic lava flows (e.g., Harris et al., 2004).

Likewise, Flynn and Mouginis-Mark (1995), Harris et al. (1997b) and Carn and Oppenheimer (2000) have applied "spectral feature space" classifications using two bands of spectral satellite data for the same phenomena. Thus, the same classification methods proposed for Io can be applied to Earth, with the advantage that it is simpler to test the classifications on Earth. In this section, we select a range of well-observed terrestrial eruptions of different styles and subject them to the same type of analysis as the ionian eruptions, concentrating on the validity of the 2:5-µm emission ratio as a means of classification.

4.1. Comparison of lava cooling on Earth and Io

The major difference between Io and the Earth is the presence of a substantial atmosphere on Earth. The atmosphere has a significant effect on the longer-term cooling of lava surfaces, but does not substantially alter the initial few minutes of cooling (e.g., Keszthelyi and McEwen, 1997). This can be more clearly seen when comparing the position of the peak emission wavelength as a function of time (Fig. 7). Overall, the reasoning for choosing 2 µm as the optimal short wavelength is unaffected by the environmental differences between the Earth and Io. The longer wavelength should ideally be somewhat shorter on the Earth than Io, but 4 to 5 µm provides a good compromise to cover a range of eruption styles.

Fig. 8. a) shows the ratio of the 2-µm radiant flux to the radiant flux at other wavelengths (*x* µm) for a selection of probable insulated flows on Io. The smaller the ratio, the greater the difference between the 2 µm output and the larger radiant flux at the selected wavelength. The original radiant fluxes were generated from fits to NIMS spectra of thermal emission from these volcanoes obtained 26 June 1996 (Orbit G1): see Davies (2003b). For Prometheus, a temperature/area distribution of 50.4 km^2 at 437 K and 0.049 km^2 at 1263 K fit the data and are used to generate this curve. The smallest ratios are found with a numerator value of 5.5 to 7.0 µm (hollow symbols), outside of the NIMS range (0.7 to 5.2 µm). While a value in the range 5.5 to 7.0 µm would be one of an ideal wavelength pair to use in this particular scenario, 5 µm works almost as well with 2-µm data. b) shows similar curves to those in Fig. 8a derived from analysis of NIMS data of Pele, on Io (Davies et al., 2001), which is believed to be an active lava lake, and for terrestrial lava lakes at Erebus volcano, Antarctica (see Davies et al., 2008a) and Erta'Ale volcano, Ethiopia (see Davies, 2010). The smallest ratio (denoted by hollow symbols) is consistently between 2.5 and 4 µm, although there is little difference from ratios using 5- to 6-µm data. The narrowness of the gap between the peak ratio wavelength and 2 µm is a reflection of the steepness of the spectrum across this wavelength range. This remarkable consistency in the shape of the integrated thermal emission spectrum, despite different environmental and planetary conditions and different compositions of silicate magma, is a promising diagnostic for identifying active lava lakes in low-spatial-resolution data.

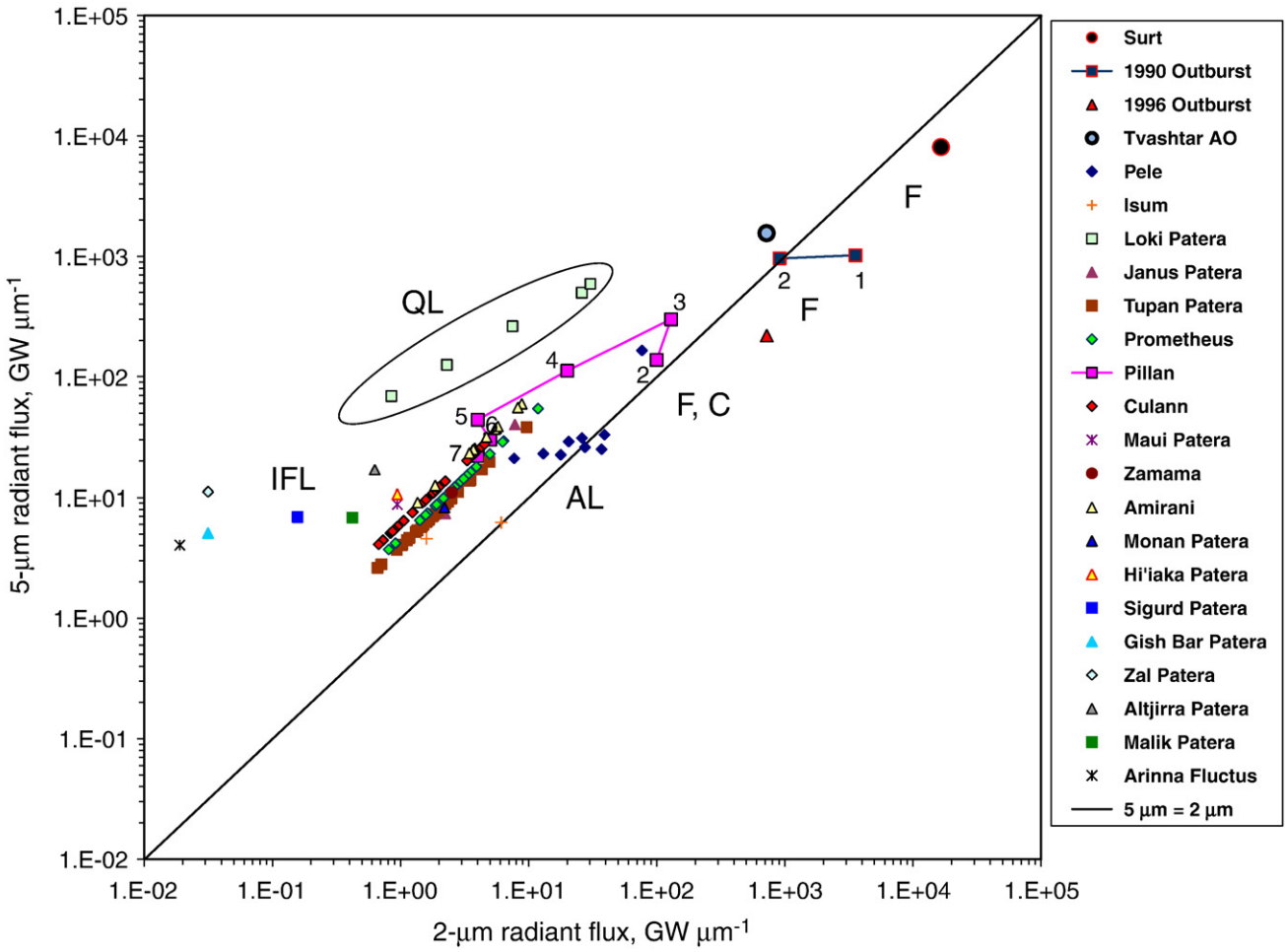

Fig. 10. Radiant fluxes at 2 and 5 µm for different volcanoes on Io. AL is the active overturning lava lake (Pele) as seen by NIMS and ground-based telescopes utilizing adaptive optics (AO). F are examples of lava fountains at Surt in 2001, Tvashtar in 2001, the Loki region in January 1990 (when thermal emission diminished from position 1 to position 2 in a few hours), and a location close to the sub-jovian point in 1996. F, C is lava fountains or open channel flow at Pillan during 1997–1999. The time sequence for Pillan is numbered 2–7, with 2 being the earliest observation. The numbers correspond to the Pillan spectra in Fig. 3. IFL indicates insulated (tube-fed) pahoehoe flows at Prometheus, Amirani, Zamama and other locations, and possible quiescent or occasionally active lava lakes (e.g., Tupan Patera, and Isum). QL is the quiescent lava "sea", a massive lava lake, of Loki Patera. Rough groupings by lava emplacement mode are shown. The distance from the 2-µm = 5-µm radiant flux line (i.e., 2:5 µm = 1) is an indication of the thermal intensity of volcanic activity: lava fountains and vigorously-overturning lava lakes are close to, on, or below the line, whereas insulated flows are above and further from it. Eruptions located to the left of the 2-µm = 5-µm radiant flux line have a decreasing ratio of hot surfaces to cool surfaces, and, by implication, the vigour of the eruption decreases with increasing distance from the line. To the right of the line, eruption vigour increases with increasing distance from the line, with violent eruptions exposing large areas at very high temperatures. The general temporal trend for any high-energy eruption would be to the left in this graph, as surfaces cool. Any renewal of activity would increase the 2:5-µm radiant flux ratio and move a datum to the right.

4.2. Thermal remote-sensing data available for the Earth

While the 2:5-µm emission ratio is theoretically as good a metric for the study of volcanoes on Earth as on Io, it would be useless if directly applied to Earth. A water absorption band extends between 4 and 8.6 µm, so surface emission cannot be detected from space over much of this wavelength range. There is a narrow band at 4.8 µm of roughly 70% atmospheric transmission, and other nearby atmospheric windows within which the atmosphere is more transmissive, especially at 2–2.4 µm and 3.4–4 µm. These two latter wavebands are used by most orbiting remote-sensing instruments used for volcano hot spot applications (Table 3).

The most frequent observations of the Earth's surface are provided by weather satellites in geostationary orbit. For example, *GOES* images are available every 15 to 30 minutes but with only 1- to 4-km pixels and four usable bands between 0.5 µm and 12.5 µm (Table 3). *GOES* data of the north Pacific region, including Hawai'i, are obtained at 15-minute intervals and have been used to provide useful constraints on the timing of events during an eruption, with the style of the eruptive activity (effusive lava flow) being determined by field observations (Harris et al., 2000b).

The next step down in temporal resolution (but up in spatial resolution) is provided by polar-orbiting weather satellites carrying instruments such as the Advanced Very High Resolution Radiometer (AVHRR) with ~1-km pixel resolution and with between four and six bands in the 0.6 to 12.5 µm region (Table 3). Because AVHRR is flown on multiple spacecraft, observations of a given location are obtained every few (2–4) hours. AVHRR data, as well as similar data provided by the Along Track Scanning Radiometer, have been successfully used to identify and track various types of effusive activity and associated lava fountaining (Harris et al., 1997a), lava flows (Harris et al., 1997a, 2000a; Wooster and Rothery, 1997b), lava lakes (Harris et al., 1999b) and lava domes (Wooster and Rothery, 1997a).

The Moderate Resolution Imaging Spectroradiometer (MODIS) instruments on the Earth-orbiting *Terra* and *Aqua* spacecraft provide a combination of moderately high temporal, spatial, and spectral resolution. Equatorial targets are imaged four times a day. High-latitude targets are imaged at a higher frequency. Each MODIS sensor collects data at 36 visible-to-thermal infrared wavelengths (spanning 0.405 to 14.385 µm) at spatial resolutions of 250 to 1000 m (Wright et al., 2004). As with AVHRR, MODIS data have been shown to be valuable in providing eruption detections and subsequent time-series

Table 3
Low-spatial-resolution orbital infrared observations of the Earth.

Spacecraft	*GOES*[a]	*NOAA*[b]	*Terra/Aqua*[c]
Instrument	Imager	AVHRR	MODIS
Repeat time	≤30 min	2–4 h	~6 h or less
Spatial resolution	1–4 km [a]	1.1 km	0.25–1.0 km
Spectral range (μm)	0.55–12.5	0.58–12.5	0.405–14.385
Number of bands	5 [a]	6	36
2-μm band?	No (~0.6 μm)	Yes (~1.6 μm)	Yes (~2.1 μm)
5-μm band?	No (~3.9 μm)	No (~3.7 μm)	No (~4.5 μm—for clouds; ~3.9 μm for fires and volcanoes)

[a] Synchronous Meteorological Satellite-*GOES* series began in 1974 and currently has 4 operational satellites (*GOES 10–13*). It did not, however, begin to carry the Imager until 1994. The *GOES* Imager has one visible and four thermal infrared bands. Band 3 is a moisture detection band with a resolution of 8 km pixel^{-1} and is not suitable for observing volcanic thermal emission.
[b] *NOAA* Series first began carrying AVHRR in 1978 and currently has 5 operational satellites (*NOAA 10, 14–17*). Tabulated information is for *NOAA 15–17*.
[c] *Terra*-MODIS launched in December 1999, *Aqua*-MODIS in May 2002.

data for a range of active volcanic phenomena (e.g., Rothery et al., 2005; Wright et al., 2004; Wright and Pilger, 2008).

Higher spatial resolution is provided by other instruments, such as ASTER on the *Terra* spacecraft, *Landsat*'s Thematic Mapper (TM) and Enhanced Thematic Mapper Plus (ETM+), and the Hyperion hyperspectral imager and Advanced Land Imager (ALI) on the *Earth Observing 1* (*EO-1*) spacecraft. The ASTER, *Landsat* TM and *Landsat* ETM+ instruments typically can image a specific volcano only twice every ~16 days (one day and one night observation), but at spatial resolutions of 15 to 120 m. Time-series data collected by TM have shown cyclic lava dome extrusion (Oppenheimer et al., 1993a), the thermal structure of active 'a'a and pahoehoe flow surfaces (Flynn et al., 1994; Oppenheimer, 1991), as well as fountain-fed flows (Wright et al., 2001), lava lakes (Harris et al., 1999a) and highly

Table 4
Thermal characteristics of different active volcanoes on Io and Earth.[a]

Ionian volcanoes			Terrestrial volcanoes		
Eruptive Style	Center	Thermal emission characteristics	Eruptive Style	Center	Thermal emission characteristics
Lava lake	Pele	Steady, fixed emission 210–280 GW (~15 kW m^{-2})	Lava lake	Erebus, Antarctica, 1985 and 2005 Erta'Ale, Ethiopia 1973, 2009	Steady emission 0.02 GW (28 kW m^{-2}) Steady emission up to 3.5 GW (50 kW m^{-2})
Lava fountains and open channel flow; transition to insulated sheet flows	Pillan 1997	Dropped from 3600 GW to 350 GW as hottest area decreased from 30 to 0.5 km^2 (~32 kW m^{-2})	Open channel and tube-fed 'a'a flows	Etna, Italy, 1992, 2004 (single channel)	Peaked at 0.5 GW, dropped to 0.1 GW in 4 days (20.8 to 5.9 kW m^{-2}).
Insulated flow field	Prometheus	Variable thermal emission, typically ~100 GW (~2 kW m^{-2}). Moved 80 km in 20 years	Tube-fed pahoehoe	Kilauea, Hawai'i, 1991	Thermal emission typically 0.2–0.3 GW (3–4 kW m^{-2})
Insulated flow field	Amirani	Variable thermal emission, typically 300 GW (~2 kW m^{-2}). Source shifted ~100 km	Lava fountains and fountain-fed sheet flow	Krafla, Iceland, 1984	26–50 GW (~0.5–1.5 kW m^{-2})
Large active patera	Loki Patera	Periodic activity for many years: regular brightenings. Average 13 TW (~0.3 kW m^{-2}), from 2.1×10^4 km^2	Large active lava lake (>10 km in diameter)	No terrestrial equivalent	–
Insulated 'a'a lava flow	No ionian equivalent	–	Insulated 'a'a lava flow	Lonquimay, Chile, 1989	0.1 GW (3.2 kW m^{-2})
Insulated silicic lava flow	No ionian equivalent	–	Insulated silicic lava flow	Santiaguito, Guatemala, 2000	0.15 GW (0.5–1.2 kW m^{-2})
Lava dome	No ionian equivalent		Lava dome	Lascar, Chile, 1991	~0.06 GW (2–3 kW m^{-2})

After Keszthelyi et al. (2001).
Notes. [a] See also Table 2 of Harris et al. (2002) for the typical thermal character of a range of terrestrial effusive phenomena.
Data sources—Io:
Pele: Davies et al. (2001).
Pillan: Davies et al. (2001).
Prometheus: Davies et al. (2006b).
Amirani: Davies (2003b).
Loki Patera: Matson et al. (2006).
Data sources—Earth:
Erebus: Harris et al. (1999b) and Davies et al. (2008a).
Erta'Ale: Harris et al. (1999a), Davies (2010).
Etna, 1992: Harris et al. (1997a), Wright et al. (2010).
Kilauea, 1991: Harris et al. (1998).
Krafla, 1984: Harris et al. (1995).
Lonquimay, 1989: Oppenheimer (1991).
Santiaguito, 2000: Harris et al. (2002).
Lascar, 1991: Oppenheimer et al. (1993a).

Table 5a
Mean values for feature surface thermal structure calculated using TM data.

Location and image date	Feature type	Feature area, (km^2)	Th, °C (assumed)	Tc, °C (calculated)	fh, (calculated)	fc, (calculated)
Erebus: 26-Jan-1985	Lava lake	0.0002	1000	788	0.00000	1.00000
Erebus: 29-Jan-1989	Lava lake	0.0003	1000	397	0.13000	0.87000
Erta 'Ale: 5-Jan-1986	Lava lake	0.0028	1100	351	0.02000	0.98000
Pu'u 'O'o: 26-Jul-1991	Lava lake	0.0040	1000	847	0.02500	0.97500
Santiaguito: 25-Oct-1987	Silicic lava flow	0.2336	927	91	0.00005	0.99995
Santiaguito: 5-Oct-1988	Silicic lava flow	0.0895	830	193	0.00006	0.99994
Santiaguito: 16-Jan-1990	Silicic lava flow	0.0435	830	124	0.00008	0.99992
Santiaguito: 19-Jan-1990	Silicic lava flow	0.0251	275	120	0.00000	1.00000
Santiaguito: 8-Jul-1991	Silicic lava flow	0.0086	830	204	0.00029	0.99971
Santiaguito: 22-Apr-1992	Silicic lava flow	0.0300	830	180	0.00069	0.99931
Santiaguito: 8-May-1992	Silicic lava flow	0.0234	830	211	0.00099	0.99901
Santiaguito: 10-Jul-1992	Silicic lava flow	0.0152	830	213	0.00249	0.99751
Santiaguito: 23-Oct-1992	Silicic lava flow	0.0340	830	159	0.00044	0.99956
Santiaguito: 19-Jan-1993	Silicic lava flow	0.0500	830	164	0.00014	0.99986
Santiaguito: 12-Feb-1993	Silicic lava flow	0.0391	830	172	0.00035	0.99965
Santiaguito: 13-Dec-1993	Silicic lava flow	0.0085	830	186	0.00072	0.99928
Santiaguito: 4-Apr-1994	Silicic lava flow	0.0132	830	175	0.00045	0.99955
Santiaguito: 29-Oct-1994	Silicic lava flow	0.0653	894	135	0.00129	0.99871
Santiaguito: 9-Feb-1995	Silicic lava flow	0.0477	856	121	0.00006	0.99994
Santiaguito: 21-Feb-1996	Silicic lava flow	0.0219	830	255	0.00036	0.99964
Santiaguito: 24-Mar-1996	Silicic lava flow	0.0545	830	120	0.00002	0.99998
Santiaguito: 23-Jan-2000	Silicic lava flow	0.0927	830	138	0.00032	0.99968
Santiaguito: 25-Jan-2001	Silicic lava flow	0.0712	830	194	0.00056	0.99944
Lascar: 07-Jan-1990	Dome	0.0216	900	196	0.00027	0.99973
Lascar: 25-Mar-1990	Dome	0.0207	900	171	0.00018	0.99982
Popocatepetl: 21-May-1996	Dome	0.0162	900	174	0.00068	0.99932
Popocatepetl: 12-Oct-1996	Dome	0.0189	900	178	0.00081	0.99919
Popocatepetl: 29-Nov-1996	Dome	0.0090	900	183	0.00058	0.99942
Popocatepetl: 18-Mar-1999	Dome	0.0162	900	195	0.00023	0.99977
Popocatepetl: 2-Feb-2000	Dome	0.0126	900	176	0.00060	0.99940
Nyiragongo: 7-Aug-1997	Lava lake	0.000025	–	–	–	–

Th = hot component temperature.
Tc = cool or crust component temperature.
fh = fraction of pixel at temperature Th.
fc = fraction of pixel at temperature Tc.
Popocatepetl results are obtained by applying the method of Flynn et al. (1994) to each image. Other results are derived as follows:
(1) Lonquimay data are from Oppenheimer (1991).
(2) Lascar data are from Oppenheimer et al. (1993a).
(3) Lava lake data are from Harris et al. (1999a and 1999b).
(4) Santiaguito results are obtained using the method of Harris et al. (2003) so Th is not assumed.
(5) Nyiragongo data from Harris et al. (1999b).

insulated silicic lava flows (Harris et al., 2004). Because the *EO-1* spacecraft is pointable, Hyperion and ALI can have better temporal coverage than ASTER, and are theoretically capable of obtaining up to 10 observations in a 16-day period. Data have been collected from a wide range of volcanic eruptions, including lava domes and lava flows (Davies et al., 2008b, 2006a; Wright et al., 2010) and lava lakes (Davies et al., 2008a).

4.3. Comparison of thermal signatures on Earth and Io

In this section we compare various aspects of the thermal signatures of similar styles of eruption on Io and Earth. We consider not only a synthesized 2:5-μm emission ratio, but also the absolute magnitude of the power output, temporal evolution of the radiance trend, and spatial pattern of the thermal emission. As we are focused on low-spatial-resolution data, where the entire emitting area of the volcanic eruption is sub-pixel, we can make use of available high-spatial-resolution data to synthesize the integrated thermal emission spectrum, as if the entire eruption were sub-pixel. Before this process is described, we start with a brief discussion of selected terrestrial eruptions before compiling the results.

Eruption types are here classified as lava fountains, lava lakes, channel-fed flows, insulated (tube-fed and well-crusted) basaltic lava flow fields, lava domes and very well-insulated silicic flows. Table 4 shows the observed thermal characteristics of different active volcanoes on Earth, and equivalents on Io.

Table 5b
Kilauea and Lonquimay (extended-source) thermal structure.[a]

Location–date	Feature type	Radiant thermal emission, (MW)	Total emitting area, (km^2)	Radiant flux density, ($kW\ m^{-2}$)	2-μm radiant flux, ($MW\ \mu m^{-1}$)	5-μm radiant flux, ($MW\ \mu m^{-1}$)	2:5-μm radiant flux ratio
Kilauea 23-Jul-1991	Pahoehoe	1144	0.38	3.02	5.30	115.02	0.046
Kilauea 11-Oct-1991	Pahoehoe	3268	1.11	2.94	14.65	324.68	0.045
Kilauea 14-Feb-2000	Pahoehoe	1572	0.48	3.28	6.69	163.08	0.047
Kilauea 31-Jan-2001	Pahoehoe	1076	0.35	3.09	4.23	108.49	0.039
Lonquimay 8-Sep-1989	Insulated 'a'a	1125	0.035	3.21	0.356	11.593	0.027

[a] Data derived from fitting temperatures to each pixel (see text) and then summing the resulting spectra to yield the integrated thermal emission spectra in Fig. 12, 2- and 5-μm radiant fluxes, and radiant flux densities.

Table 5c
Etna open channel flow thermal structure from Hyperion data—12–16 September 2004.[a]

Date	Radiant thermal emission, (MW)	Total emitting area,[b] (m^2)	Radiant flux density, ($kW\ m^{-2}$)	2-μm radiant flux, ($MW\ \mu m^{-1}$)	5-μm radiant flux, ($MW\ \mu m^{-1}$)	2:5-μm radiant flux ratio
Etna 12-Sep-2004	305	14,680	20.8	38.4	39.3	0.98
Etna 14-Sep-2004	499	25,805	19.3	67.4	62.6	1.08
Etna 16-Sep-2004	143	24,117	5.9	11.5	17.0	0.68

[a] Calculated from data in Wright et al. (2010).
[b] Percentages of flow surface area at different temperatures are given in Fig. 7 of Wright et al. (2010).

We next use an archive of remote sensing (e.g., TM and ETM+ and Hyperion data) and *in situ* data covering the full range of active effusive features considered here. The features are listed in Tables 5a, 5b and 5c. For volcanoes listed in Tables 5a and 5b, except as noted, the thermal structure of each pixel is assessed following the method of Flynn et al. (1994). For each hot pixel in the TM/ETM+ image of the eruption, the method of Flynn et al. (1994) was applied to obtain, from each pixel-integrated temperature, the fraction (fh) of the pixel area (a full pixel covers 900 m^2) occupied by a hot source at an assumed temperature (Th), as well as the cooler crust temperature (Tc). Following, for example, the method of Glaze et al. (1989), these fractional values can then be converted to radiant flux densities ($kW\ m^{-2}$), and then to expected (feature-integrated) 2- and 5-μm radiant fluxes. Results for the data in Table 5a, where a mean value is used for Tc, are given in Table 6. An alternative method was used for Kilauea and Lonquimay (Table 5b). For these two volcanoes, values were calculated by integrating the thermal emission spectra having derived Tc on a pixel-by-pixel basis, rather than using a mean Tc value. Comparable thermal emission data are given for ionian volcanoes in Table 7. 2- and 5-μm radiant flux values are plotted in Fig. 11. Table 5c shows results for Etna derived from Hyperion data.

With these characteristics it is possible to examine the evolution of thermal emission spectra for each eruption style as seen in low-spatial-resolution data, as has been done for the ionian cases described above.

4.3.1. Fountains and channel-fed flows

Given the brief lifetime of fountaining events (typically just a few hours), space-based observations of lava fountains on Earth are extremely rare. For those events that have been captured, the intensity of the thermal emission typically saturates detectors operating in the short-wave infrared, as well as in the mid- and thermal infrared. However, emission is sufficiently intense to show up in the near-infrared (i.e., around 1 μm). Harris et al. (1997b) describe AVHRR observations of fountain-fed flows during the September 1984 eruption of Krafla, Iceland. Data were saturated at 3 μm and between 10 and 12 μm, but a strong thermal signal was observed at 1.1 μm. Likewise, Wright et al. (2001) considered an ETM+ image of fountain-fed flows active at Etna during October 1999 (unfortunately, with much of the data saturated over multiple wavelengths), with Harris and Neri (2002) also considering AVHRR time-series data (at thermal infrared wavelengths) for the same eruption. Both events fed channelized lava flows.

Wright et al. (2010) examined an open channel 'a'a flow on Etna in 2004 that was observed by *EO-1* Hyperion. The eruption began on 7 September 2004 with the opening of a vent at the base of the South East Crater. Observations obtained on 12, 14 and 16 September 2004 showed two flows that were erupted on 10 and 13 September 2004, respectively. The larger 10 September flow had a well-defined central channel when observed on 12 September 2004 (Wright et al., 2010). Because Hyperion data are hyperspectral, temperature derivation was possible for all

Table 6
Thermal properties calculated from Table 5a.

Location and image date	Feature type	Effective radiation temperature, (°C)	Radiant flux density, ($kW\ m^{-2}$)	Total radiated power, (GW)	2-μm radiant flux, ($MW\ \mu m^{-1}$)	5-μm radiant flux, ($MW\ \mu m^{-1}$)	2:5-μm radiant flux ratio
Erebus: 26-Jan-85	Lava lake	846	89.0	0.02	3.410	1.78	1.9108
Erebus: 29-Jan-89	Lava lake	646	40.4	0.01	1.394	1.64	0.8511
Erta 'Ale: 5-Jan-86	Lava lake	317	6.9	0.02	0.165	2.57	0.0643
Pu'u 'O'o: 26-Jul-91	Lava lake	854	91.6	0.37	79.364	40.46	1.9615
Santiaguito: 25-Oct-87	Silicic lava flow	91	1.0	0.23	0.007	10.36	0.0007
Santiaguito: 5-Oct-88	Silicic lava flow	193	2.7	0.24	0.206	22.31	0.0092
Santiaguito: 19-Jan-90	Silicic lava flow	120	1.4	0.03	0.003	1.99	0.0017
Santiaguito: 16-Jan-90	Silicic lava flow	124	1.4	0.06	0.007	3.75	0.0019
Santiaguito: 8-Jul-91	Silicic lava flow	204	2.9	0.03	0.029	2.49	0.0116
Santiaguito: 22-Apr-92	Silicic lava flow	183	2.4	0.07	0.049	6.52	0.0075
Santiaguito: 8-May-92	Silicic lava flow	214	3.2	0.07	0.106	7.65	0.0138
Santiaguito: 10-July-92	Silicic lava flow	220	3.4	0.05	0.083	5.35	0.0154
Santiaguito: 23-Oct-92	Silicic lava flow	160	2.0	0.07	0.025	5.35	0.0046
Santiaguito: 19-Jan-93	Silicic lava flow	164	2.1	0.10	0.042	8.32	0.0050
Santiaguito: 12-Feb-93	Silicic lava flow	173	2.3	0.09	0.046	7.45	0.0062
Santiaguito: 13-Dec-93	Silicic lava flow	188	2.6	0.02	0.017	1.99	0.0084
Santiaguito: 4-Apr-94	Silicic lava flow	176	2.3	0.03	0.017	2.61	0.0066
Santiaguito: 29-Oct-94	Silicic lava flow	143	1.7	0.11	0.024	7.77	0.0030
Santiaguito: 9-Feb-95	Silicic lava flow	121	1.4	0.07	0.007	3.85	0.0017
Santiaguito: 21-Feb-96	Silicic lava flow	255	4.4	0.10	0.314	11.38	0.0276
Santiaguito: 24-Mar-96	Silicic lava flow	120	1.3	0.07	0.007	4.30	0.0016
Santiaguito: 23-Jan-00	Silicic lava flow	140	1.6	0.15	0.029	10.43	0.0028
Santiaguito: 25-Jan-01	Silicic lava flow	195	2.7	0.19	0.179	18.41	0.0097
Lascar: 7-Jan-90	Dome	197	2.8	0.06	0.057	5.69	0.0100
Lascar: 25-Mar-90	Dome	172	2.2	0.05	0.023	3.86	0.0060
Popocatepetl: 21-May-96	Dome	178	2.3	0.04	0.023	3.31	0.0068
Popocatepetl: 29-Nov-96	Dome	186	2.5	0.02	0.017	2.05	0.0081
Popocatepetl: 12-Oct-96	Dome	182	2.4	0.05	0.031	4.10	0.0075
Popocatepetl: 18-Mar-99	Dome	197	2.8	0.04	0.043	4.27	0.0100
Popocatepetl: 2-Feb-00	Dome	179	2.4	0.03	0.018	2.61	0.0070
Nyiragongo: 07-Aug-87	Lava lake	365	9.4	0.0025	0.004	0.03	0.1115

Table 7
Thermal emission parameters for different classes of ionian eruptions included in this analysis.

Location	Date	Eruption style/ interpretation	2-μm radiant flux, (GW μm^{-1})	5-μm radiant flux, (GW μm^{-1})	2-μm delta, (GW μm^{-1})	2-μm delta as % of 2-μm flux	Radiant flux density, (kW m^{-2})	2:5-μm radiant flux ratio	References
1990 Outburst 1 (GB)	09-Jan-90	Lava fountains	3550	1020	−2530	−71.3	70.6	3.48	Blaney et al. (1995); Davies (1996)
1990 Outburst 2 (GB)	09-Jan-90	Lava fountains and clastogenic flows	910	960	50	5.5	7.9	0.95	Blaney et al. (1995); Davies (1996)
1996 Outburst (GB)	06-Oct-96	Lava fountains	723	220	−502	−69.6	287.0	3.29	Stansberry et al. (1997)
2001 Surt (AO)	22-Feb-01	Lava fountains	16,500	8100	−8459	−51.2	97.01	2.05	Marchis et al. (2002)
2001 Tvashtar Paterae (AO)	19-Feb-01	Lava fountains and flows	717	1559	842	117.4	23.2	0.46	Marchis et al. (2001)
Pillan 2 (NIMS)	07-May-97	Lava fountains	100	138	38	38.0	32.3	0.72	Davies et al. (2001)
Pillan 3 (NIMS)	28-Jun-97	Lava fountains and channelled flows	129	300	171	132.56	1.73	0.43	Davies et al. (2001)
Pillan 4 (NIMS)	18-Sep-97	Inflating flows	20	112	92	460.00	3.37	0.18	Davies et al. (2001)
Pillan 5 (NIMS)	31-May-98	Inflating flows	4	44	40	1000.00	1.19	0.09	Davies et al. (2001)
Pillan 6 (NIMS)	20-Jul-98	Mostly cooling flows	5	30	25	500.00	1.44	0.17	Davies et al. (2001)
Pillan 7 (NIMS)	02-May-99	Mostly cooling flows	4	22	18	450.00	1.52	0.18	Davies et al. (2001)
Pele (NIMS)	06-Sep-96	Lava lake	37	25	−12	−32.4	34.10	1.48	Davies et al. (2001)
Pele (NIMS)	07-May-97	Lava lake	13	23	10	76.9	6.37	0.57	Davies et al. (2001)
Pele (NIMS)	18-Sep-97	Lava lake	26	31	5	19.2	9.35	0.84	Davies et al. (2001)
Pele (NIMS)	31-May-98	Lava lake	27	26	−1.5	−5.5	13.71	1.06	Davies et al. (2001)
Pele (NIMS)	20-Jul-98	Lava lake	39	33	−6	−15.4	16.92	1.18	Davies et al. (2001)
Pele (NIMS)	02-May-99	Lava lake	20.50	29.00	8.50	41.5	9.24	0.71	Davies et al. (2001)
Pele 1 (AO)	26-Dec-01	Lava lake	17.78	22.48	4.70	26.4	31.88	0.79	Marchis et al. (2005)
Pele 2 (AO)	28-Dec-01	Lava lake	7.68	20.99	13.30	173.1	14.86	0.37	Marchis et al. (2005)
Pele (IRIS)	09-Jul-79	Lava lake	76.5	165.2	88.63	115.8	6.31	0.46	Pearl and Sinton (1982)
Pele (IRIS, NIMS, AO)	1996–2001	Lava lake (9)	29.44	41.74	12.29	44.41	15.86	0.81	Pearl and Sinton (1982), Davies et al. (2001), Marchis et al. (2005)
Isum 2 (AO)	28-Dec-01	Lava lake or lava fountains	6.11	6.23	0.12	2.0	40.31	0.98	Marchis et al. (2005)
Tupan Patera (NIMS, AO)	1996–2001	Insulated flow or lake (27)	2.25	8.81	6.56	295.7	2.73	0.25	Ennis and Davies (2005), Davies (2003b), Marchis et al. (2005)
Janus Patera 1 (AO)	20-Dec-01	Insulated flow or crusted lake	2.23	7.42	5.19	232.6	12.26	0.30	Marchis et al. (2005)
Janus Patera 2 (AO)	22-Dec-01	Insulated flow or crusted lake	7.80	40.20	32.41	415.7	8.08	0.19	Marchis et al. (2005)
Isum 1 (AO)	26-Dec-01	Insulated flow or crusted lake	1.59	4.57	2.97	187.1	14.36	0.35	Marchis et al. (2005)
Hi'iaka Patera (NIMS)	28-Jun-96	Insulated flow or crusted lake	0.94	10.68	9.74	1033.3	2.51	0.09	Davies (2003b)
Sigurd Patera (NIMS)	28-Jun-96	Insulated flow or crusted lake	0.16	6.91	6.76	4300	2.31	0.02	Davies (2003b)
Gish Bar Patera (NIMS)	28-Jun-96	Insulated flow or crusted lake	0.03	5.09	5.06	16,100	2.47	0.006	Davies (2003b)
Zal Patera (NIMS)	28-Jun-96	Insulated flow or crusted lake	0.03	11.15	11.12	35,400	3.15	0.003	Davies (2003b)
Arinna Fluctus (NIMS)	28-Jun-96	Insulated flow or crusted lake	0.02	4.05	4.03	21,294	1.99	0.0047	Davies (2003b)
Malik Patera (NIMS)	28-Jun-96	Insulated flow or crusted lake	0.42	6.84	6.42	1529	6.75	0.06	Davies (2003b)
Zamama (NIMS)	1996–1999	Insulated flows (24)	1.16	9.30	8.13	698.8	2.45	0.13	Ennis and Davies (2005), Davies (2003b)
Culann (NIMS)	1996–1999	Insulated flows (28)	1.84	11.20	9.35	507.8	1.99	0.16	Ennis and Davies (2005), Davies (2003b)
Amirani (NIMS)	1996–2001	Phh tube-fed flows (13)	4.60	31.03	26.43	575.0	1.88	0.15	Ennis and Davies (2005), Davies (2003b)
Prometheus (NIMS)	1996–2001	Phh tube-fed flows (29)	3.09	14.18	11.09	359.0	2.20	0.22	Davies et al. (2006b)
Loki Patera (NIMS)	05-Apr-97	Lava lake (magma sea?)	26.00	499.46	473.46	1820.7	0.40	0.05	Matson et al. (2006)
Loki Patera (NIMS)	25-Jun-97	Lava lake (magma sea?)	30.28	591.25	560.97	1852.9	0.48	0.05	Matson et al. (2006)
Loki Patera (NIMS)	21-Jul-98	Lava lake (magma sea?)	2.30	125.52	123.22	5359.9	0.10	0.02	Matson et al. (2006)
Loki Patera (NIMS)	30-Jun-99	Lava lake (magma sea?)	0.85	69.09	68.25	8051.9	0.06	0.01	Matson et al. (2006)
Loki Patera (NIMS)	28-Dec-00	Lava lake (magma sea?)	7.48	262.80	255.32	3413.1	0.22	0.03	Matson et al. (2006)
Loki Patera (NIMS)	1997–2000	Lava lake—average (5)	13.38	309.63	296.24	4099.7	0.25	0.03	Matson et al. (2006)
Altjirra Patera (NIMS)	28-Jun-96	Insulated flow	0.94	16.97	16.34	2600.0	0.01	0.06	Davies (2003b)

Notes:
(1) Numbers in brackets are the number of observations that are averaged.
(2) For Loki Patera, the low-albedo, thermally active area is taken as 2.1×10^4 km^2 (Matson et al., 2006).
(3) "2-μm delta" is distance (in units of GW μm^{-1}) from datum to the 2-μm = 5-μm line.
(4) NIMS = *Galileo* Near Infrared Mapping Spectrometer; AO = Adaptive Optics; GB = ground-based telescope. IRIS = *Voyager* Infrared Radiometer Interferometer Spectrometer.
(5) Phh = pahoehoe.

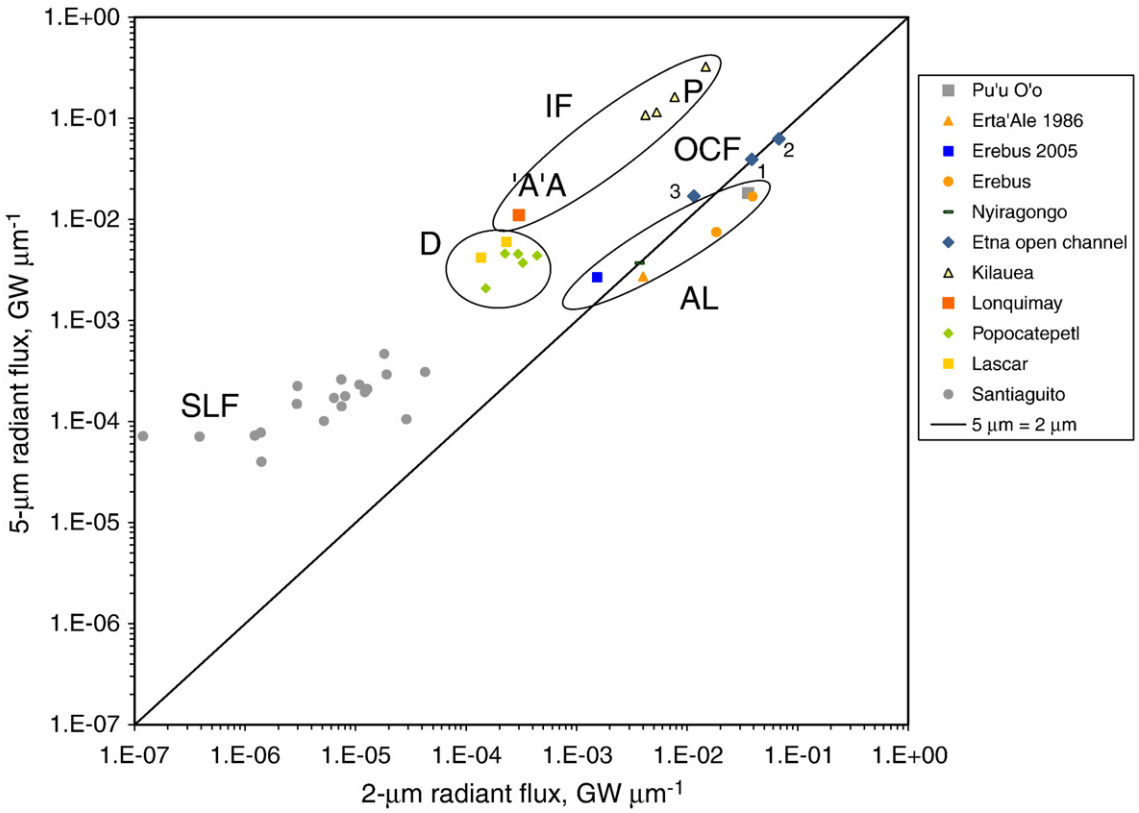

Fig. 11. Radiant fluxes at 2 and 5 µm for different volcanoes on Earth. Key: AL are actively overturning lava lakes. IF are insulated (tube-fed pahoehoe) flows (P) (Kilauea—see text for caveats) and insulated 'a'a flows ('A'A) (Lonquimay). OCF is an open channel flow at Etna in 2004. There is a cluster of data for silicic domes (D) at Popocatepetl and Lascar. SLF is for a highly silicic insulated flow (Santiaguito). Like the ionian examples of Fig. 10, the proximity to the 2-µm = 5-µm radiant flux line is an indication of the thermal intensity of the eruption: for example, the actively overturning lava lakes (e.g., Erebus) are located close to the line, like Pele on Io, whereas the insulated flow cases are further from it. Note that the largest terrestrial eruption yields less thermal output than the smallest ionian eruption that is included in this analysis.

emitting surfaces because there were always shorter-wavelength data that could be used in the event of saturation at longer wavelengths, avoiding multiple-band saturation problems commonly encountered with Landsat TM and ETM+.

Wright et al. (2010) determined the temperature and area distribution of this open channel flow. Derived temperatures ranged from areas of <100 °C (373 K) to >1050 °C (1323 K). The total radiant thermal emission peaked at 499 MW on 14 September 2004 (Wright

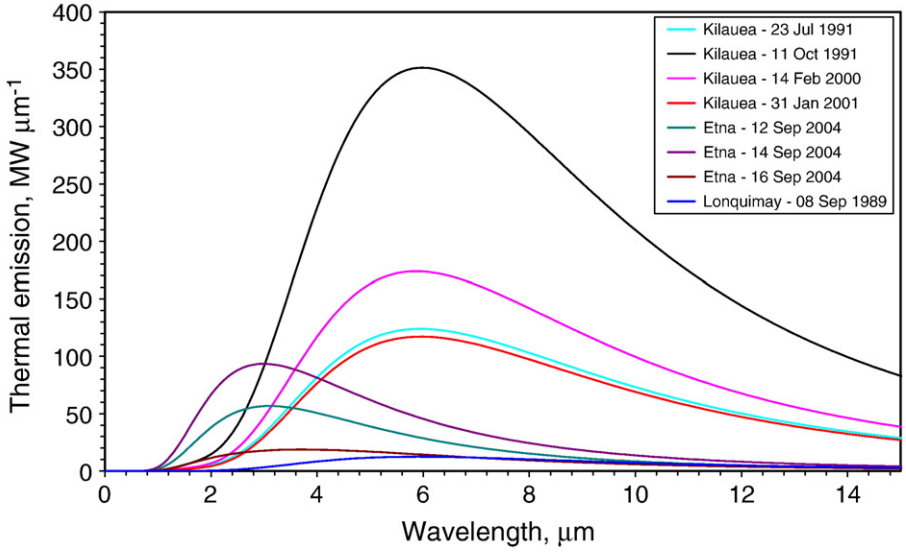

Fig. 12. Integrated thermal emission spectra from terrestrial eruptions at Kilauea in 1991, 2000 and 2001 (tube-fed pahoehoe), Etna in 2004 (channel-fed 'a'a), and Lonquimay in 1989 (well-insulated 'a'a). The Kilauea spectra were created from thermal data extracted by us from *Landsat* TM and ETM+ data. The Etna data come from temperature-area histograms produced from Hyperion data by Wright et al. (2010). The Lonquimay data are taken from Oppenheimer (1991). See text for caveats regarding use of the Kilauea and Lonquimay data.

et al., 2010), when the total emitting area was ≈25,800 m^2. Thermal structure of the flow from 12 to 16 September 2004 is summarised in Table 5c, and integrated thermal emission spectra are shown in Fig. 12. Over the three days, radiant flux density fell from 20.8 kW m^{-2} to 5.9 kW m^{-2} as the effusion rate declined, the channel reduced in area, and the emplaced flow surfaces cooled. As expected for an open channel flow, the 2:5-μm emission ratio was initially high (~1), but had already fallen to 0.68 on 16 September 2004 as activity declined.

These are data for a single active open channel flow. In a low-spatial-resolution observation where all activity is confined within a single pixel (the usual case with Io observations), the presence of other flows that are older, and therefore cooler, would increase the integrated 5-μm radiant flux to a greater amount than the 2-μm radiant flux, leading to a lower integrated radiant flux density and 2:5-μm radiant flux ratio.

Other open channel flows have similar flux densities. A 1984 Mauna Loa, Hawai'i, channelled flow had a radiant flux density of 11 to 26 kW m^{-2} (Harris et al., 2002). Channel flows on Kilauea, Hawai'i, between 1992 and 1997 typically had flux densities of 34.9 to 76.3 kW m^{-2} (see Table 2 in Harris et al., 2002). Field measurements made during 30–31 May 2001 of an open channel flow on Etna revealed surface temperatures for active lava in a small channel of between 930 and 1070 K over its first 70 m, with a correspondingly high radiant flux density of 50 kW m^{-2} (Harris et al., 2005). These numbers are comparable with the radiant flux density of 32 kW m^{-2} observed during the early stages of the Pillan eruption in May 1997 (Davies et al., 2001).

The Etna data also exhibit the beginning of the trend seen in the Pillan data, where peak thermal emission and radiant flux density decrease with time as surfaces cool and the eruption dies down. As shown in Fig. 12, open channel flows have very different thermal emission spectra from those of pahoehoe flows.

4.3.2. Lava lakes

Particularly well-studied active lava lakes include those within Halema'uma'u crater (Kilauea volcano, Hawai'i) prior to 1924, the Kupaianaha lava lake (also Kilauea from 1986 to 1990), as well as at Erebus (Antarctica), Erta'Ale (Ethiopia), and Nyiragongo (Democratic Republic of the Congo) volcanoes. In 2003 a previously unknown lava lake on Saunders Island (South Sandwich Islands), with a typical power output of 50–100 MW, was discovered in MODIS data (Patrick et al., 2005). This feature was intermittently active from 1995 through 2005, and has been inactive since December 2006.

Intensive spectroradiometer observations over the lifetime (1986–1990) of Kupaianaha's lake by Flynn et al. (1993) revealed three stages of surface activity. Stage 1 was characterised by active lava fountains and rifting, resulting in the highest thermal emission from the lake, with radiant flux densities of 22 kW m^{-2}. Stage 2 was marked by rifting events between crustal plates during which radiant flux densities were 5.3 kW m^{-2}. Times of quiescence, when a thickening crust covered the surface of the lake and radiant flux densities were 4.9 kW m^{-2}, were designated as Stage 3. Over 99% of the time the lava lake was quiescent.

Radiometer, pyrometer and thermal camera measurements of Erta'Ale's lava lake show similar results. Radiometer-based data of Harris et al. (2005) show periods of alternating vigorous and sluggish convection during which typical radiant flux densities are 25 kW m^{-2} and 8 kW m^{-2}, respectively (Harris, 2008). This compares with radiant flux densities of 13 kW m^{-2} obtained using pyrometer data by Burgi et al. (2002). Total radiant power outputs of 45–152 MW were obtained from thermal camera data (Oppenheimer and Yirgu, 2002; Spampinato et al., 2008).

The Erebus volcano lava lake has also been observed with high-spatial-resolution infrared cameras in 2004 and 2005 (Calkins et al., 2008; Davies et al., 2008a), as well as with ETM+, AVHRR and MODIS (Harris et al., 1999b; Wright and Pilger, 2008), and Hyperion and ALI (Davies et al., 2008a). The integrated thermal emission spectrum from the lava lake, derived from thermal camera data, yielded a 2-μm radiant flux of 1.53 MW $μm^{-1}$ and a 5-μm radiant flux of 2.67 MW $μm^{-1}$ (Davies et al., 2008a). The 2:5-μm ratio is therefore 0.573, similar to that of Pele. The radiant flux density is 29.6 kW m^{-2}, slightly higher than that of Kupaianaha stage 1 activity (22 kW m^{-2}) or Pele (6–17 kW m^{-2}: Davies et al. 2008a).

These lava lake flux densities are similar to those obtained by Harris et al. (1999a) using TM data for lava lakes at Erta'Ale, Erebus, Pu'u 'O'o (Kilauea, Hawai'i) and Nyiragongo (as given here in Table 6). These data yield radiant flux densities of between 6.9 and 91.6 kW m^{-2}, so that simulated 2- and 5-μm radiant fluxes for terrestrial lava lakes are 79.4 MW $μm^{-1}$ (Pu'u 'O'o) to 3.7 kW $μm^{-1}$ (Nyiragongo), and 40.5 MW $μm^{-1}$ (Pu'u 'O'o) to 33.3 kW $μm^{-1}$ (Nyiragongo), respectively, to give a 2:5-μm radiant flux ratio range of 1.962 to 0.064.

4.3.3. Insulated (tube-fed) flows

The most-often quoted example of insulated flows is the ongoing (1983–2010) Pu'u 'O'o-Kupaianaha eruption of Kilauea, where emplacement of tube-fed pahoehoe flow fields dominates volcanic activity, at typical effusion rates of ~4 m^3 s^{-1} (Sutton et al., 2003). These flow fields have been examined using TM and AVHRR data (Flynn et al., 1994; Harris et al., 1998), as well as thermal cameras (Wright and Flynn, 2003). The data of Flynn et al. (1994) and Harris et al. (1998) yield radiative flux densities of 5 kW m^{-2} and 3.58–4.16 kW m^{-2}. These flux densities are consistent with results we obtained from four TM and ETM+ images of this flow field between 1991 and 2001 (Table 5b). Some important caveats have to be noted. The TM and ETM+ data used to generate the spectra in Fig. 12 do not include pixels that are saturated in ETM+ bands 5 and 7 (around 2 μm). Estimates of integrated 2-μm and 5-μm radiant fluxes, radiant flux densities, and 2:5-μm radiant flux ratios derived from these Kilauea data are therefore minimum values. However, the similarity in derived radiative flux densities with those measured *in situ* (e.g., Flynn et al., 1994), confirms that thermal emission from a well-developed pahoehoe flow field is dominated by cooled crust rather than the relatively small hot areas that make up a tiny fraction (<<1%) of the entire flow field. For example, the FLIR (Forward-Looking Infrared) data collected by Wright and Flynn (2003) yield radiant flux densities for active pahoehoe lobes in the range 11–30 kW m^{-2}, but each lobe has an area of less than 1 m^2. From the ETM + data, minimum 2:5-μm radiant flux ratios range from 0.039 to 0.047 (Table 5b). The 2:5-μm radiant flux ratios for Kilauea are taken from the spectra in Fig. 12.

Favourable similarities exist between the tube-fed flow fields on Kilauea and suspected tube-fed cases on Io, despite the differences in environmental conditions between Io and Earth. If we compare radiant flux densities we obtain ~2 kW m^{-2} for Prometheus and ~3 kW m^{-2} for Kilauea in 1991 and 2000–2001 (Tables 6 and 7) (see Davies et al., 2006b). Environmental temperature difference, although ~200 K, is actually insignificant for active lava flow surfaces, which are at temperatures ranging from 600 K to more than 1400 K.

4.3.4. Lava domes

Lava domes form from dacitic and rhyolitic lava. No such features have been observed on Io. Data for lava domes at Lascar and Popocatepetl are shown in Tables 5a and 6. Because there are a small number of saturated pixels that are not included in the analysis, the same caveats described above for pahoehoe flows apply for here for domes. Oppenheimer et al. (1993a) examined 15 ETM+ observations of Lascar. Harris et al. (1997b) derived radiant flux densities of 2.2 to 2.8 kW m^{-2} from Lascar, which compares well with the Popocatepetl flux densities of 2.3 to 2.8 kW m^{-2}, also derived from *Landsat* data. Total power output from these domes is 20 to 60 MW. 2:5-μm radiant flux ratios are very low when compared with most other styles of eruption, with values in the range 0.006 to 0.01, with an average value of 0.0079. The average power output from domes included in this analysis was 41 MW.

4.3.5. Other types of effusive eruption: insulated 'a'a and silicic flows

Oppenheimer (1991) examined a TM image for a well-insulated 'a'a flow active at Lonquimay during 1989. These data are included in

the Table 5b review and show radiant flux densities associated with this second insulated form of emplacement of ~3 kW m^{-2}, i.e., identical to the well-insulated tube-fed pahoehoe mode of emplacement. The spectrum in Fig. 12 for Lonquimay was derived as described for the 1999, 2000 and 2001 Kilauea observations.

The highest degree of insulation known was encountered during the emplacement of extremely well-insulated silicic lava flows at Santiaguito in Guatemala (Harris et al., 2002; Harris et al., 2004). Here, analysis of TM and ETM+ data reveal radiant flux densities of 1–4.4 kW m^{-2}, with radiometer data giving radiant flux densities as low as 0.6 kW m^{-2}. The Santiaguito data yield some of the lowest overall simulated 2- and 5-μm spectral radiances for terrestrial cases, and the lowest average 2:5-μm radiant flux ratio of 0.007 (Table 6).

4.4. Synthesis of the Earth–Io comparison

Fig. 11 shows 2- and 5-μm data for a wide range of eruption types on Earth. Shown are eruptions at Etna (fountain-fed and channelized flows), Kilauea (insulated pahoehoe flows), and Lonquimay (insulated 'a'a flows); active lava lakes at Erebus, Pu'u 'O'o, Erta'Ale and Nyiragongo; more silicic insulated lava flows at Santiaguito; and lava domes at Popocatepetl and Lascar. As previously noted, the two latter cases (domes and silicic lava flows) are probably unlikely on Io.

As a test of a technique used to analyse similar NIMS data from Io, we fitted a two-temperature, two-area model to the integrated thermal emission spectra for Kilauea, Erebus, Erta'Ale and Lonquimay. The Io technique (Davies et al., 1997) yielded excellent fits to the terrestrial spectra.

Table 8 shows the thermal emission for a number of different hot spots on Io, as well as the implied radiant flux densities, and equivalent data for some terrestrial volcanoes. These data show that the magnitude of the thermal emission is much larger on Io than on the Earth for comparable styles of volcanic activity. However, the radiant flux density and the 2:5-μm radiant flux ratios are often similar. These are two indications that the styles of activity on Io and the Earth are similar. The larger overall magnitude on Io simply reflects the fact that the observed eruptions on Io tend to cover much larger areas than the terrestrial ones.

Table 8
Heat loss, mass eruption rates, and flux and mass densities for a selection of terrestrial and ionian volcanoes.

Volcano	Date	Total volcanic heat loss,[a] (GW)	Mass Flux[a,b], (kg s^{-1})	Thermal flux density[b], (kW m^{-2})	Mass flux density[a], (kg s^{-1} m^{-2})
Erebus[c]	13-Dec-2005	0.0235	64–93	29	0.02–0.05
Erebus[b]	26-Jan-1985	0.016–0.103	38–76	89–572	0.2–0.4
Pu'u O'o lava lake	26-Jul-1991	0.508–0.674	1553–2079	128–170	0.4–0.5
Nyiragongo[b]	Jan-1972	5.150	8162–10,350	174	0.2
Erebus[b]	Jan-1989	0.013–0.108	30–69	43–359	0.1–0.2
Erta 'Ale[b]	Jan-1973	4.728	14,902–18,204	50	0.2
Pillan 2 (G8)[d]	07-May-1997	1010	3.21×10^{6}	32[k]	0.103
Kupaianaha Stage 1[e]	Oct 87-Jan 88	0.018	41–57	~22	0.018–0.025
Pele, NIMS (E16)[d]	20-Jul-1998	280	644,000–889,000	17	0.04–0.05
Nyiragongo	07-Aug-1987	0.002–0.006	1–2	15–20	0.03–0.1
Erta 'Ale	05-Jan-1986	0.018–0.031	44–104	6–17	0.02–0.04
Pele, IRIS[f]	05-Mar-1979	1760	2.67×10^{6}–3.68×10^{6}	10	0.02–0.03
Pele, IRIS[g]	09-Jul-1979	1333	3.07×10^{6}–4.23×10^{6}	6.0	0.01–0.02
Kupaianaha Stage 2[e]	Oct 87-Jan 88	0.014	32–44	5.3	0.014–0.019
Kupaianaha Stage 3[e]	Oct 87-Jan 88	0.017	25–35	4.9	0.017–0.015
Pillan 4 (C10)[d]	18-Sep-1997	1730	3.58×10^{6}	3.4	0.017
Culann (G1)[h]	28-Jun-1996	139	270,400	2.9	0.008
Kilauea	23-Jul-1991	1.14	13,000	3.3	0.03
Kilauea	11-Oct-1991	3.3	36,000	2.9	0.03
Amirani (G1)[h]	28-Jun-1996	327	637,000	2.6	0.019
Tupan Patera (G1)[h]	28-Jun-1996	79	153,400	2.5	0.005
Zamama (G1)[h]	28-Jun-1996	126	244,400	2.4	0.005
Monan Patera (G1)[h]	28-Jun-1996	85	166,400	2.2	0.003
Pillan 3 (C9)[d]	28-Jun-1997	3610	1.15×10^{7}	1.7	0.006
Prometheus (G1)[h]	28-Jun-1996	178	228,800	2.0	0.003
Maui Patera (G1)[h]	28-Jun-1996	96	184,600	1.9	0.001
Pillan 7 (C20)[d]	02-May-1999	351	1.17×10^{6}	1.5	0.005
Pillan 5 (E15)[d]	31-May-1998	817	2.59×10^{6}	1.2	0.004
Pillan 6 (E16)[d]	20-Jul-1998	507	1.61×10^{6}	1.44	0.005
Loki Patera (C9)[i]	25-Jun-1997	13,084	3.23×10^{7}	0.62	0.0015
Loki hot spot[j]	05-Mar-1979	12,600	2.9×10^{7}–4×10^{7}	0.42	0.0009–0.001
Loki Patera (G7)[i]	05-Apr-1997	6053	1.49×10^{7}	0.29	0.0007
Loki Patera (G29)[i]	28-Dec-2000	5689	1.01×10^{7}	0.27	0.0005
Loki Patera (E16)[i]	21-Jul-1998	3295	8.13×10^{6}	0.16	0.0004
Loki Patera (C22)[i]	14-Aug-1999	1943	4.80×10^{6}	0.09	0.0002

Updated from Table 8 in Davies et al. (2001). See also Davies (2007). Terrestrial volcanoes are in *italics*.
[a]Total heat loss and thermal and mass flux density calculations include heat loss by convection for terrestrial volcanoes. Heat loss is for exposed surfaces only.
[b]Mass flux calculated using Harris et al. (1999a), Eqn. 18. See also Glaze et al. (1989).
[c]Davies et al. (2008a).
[d]Davies et al. (2001).
[e]Flynn et al. (1993).
[f]Pearl and Sinton (1982). Component of 113 km^2 at 654 K used. The component of 20,106 km^2 at 175 K would not be detected by NIMS. NIMS has a low-temperature detection limit of 180 K, as long as the source fills the NIMS field of view (Smythe et al., 1995). The 654 K and 175 K components yield the best fit to the IRIS Pele data.
[g]Pearl and Sinton (1982). A two-component fit to IRIS data yields 29.7 km^2 at 854 K and 181.5 km^2 at 454 K.
[h]Davies (2003b).
[i]*Galileo* NIMS data, Loki Patera low-albedo area = 2.1×10^{10} m^2 (Matson et al., 2006).
[j]Voyager IRIS data, using Loki Patera low-albedo area of 2.1×10^{10} m^2 (excluding "island").
[k]Corrected from Davies et al. (2001).

4.5. 2:5-μm ratio and eruption style

In Figs. 10 and 11 we plot the 2:5-μm radiant flux ratios for all cases considered above. Generally, we see a roughly linear decline in the 2:5-μm radiant flux ratio as the degree of insulation increases: the closer a point is to the origin, and the greater the perpendicular distance to the left of the 2–5-μm radiant flux line (i.e., deeper into 5-μm thermal feature classification space), the greater the degree of insulation. The greatest 2:5-μm ratios are related to cases where the fraction of high-temperature areas is greatest, implying a more vigorous style of volcanic eruption. Examples include overturning lava lakes, lava fountains, and lava channels.

Table 9 shows the ranking of a number of ionian and terrestrial volcanoes by eruption style as indicated by the 2:5-μm radiant flux ratio. Zal Patera (and also Arinna Fluctus) (Io) have the lowest ratios, implying very cool surfaces. Loki Patera (Io) is within the range 0.012 to 0.052, depending on the position in the resurfacing cycle (Matson et al., 2006; Rathbun et al., 2002). As the eruption style becomes more vigorous, the 2:5-μm radiant flux ratio increases, with active lava lakes (Pele) and open channel flows (Pillan), sometimes with lava fountains (Pillan again), having higher ratios of up to ≈1. Finally, for the massive thermal outbursts (almost certainly huge lava fountain episodes) at Surt in February 2001 (Marchis et al., 2002) and in the Loki region in January 1990 (Blaney et al., 1995; Davies, 1996; Veeder et al., 1994), for example, the 2:5-μm radiant flux ratio can exceed 2.

On Earth, where we observe lava fountains, lava lakes and lava flows, we know the relationship between 2- and 5-μm thermal emission holds.

5. Discussion of future observation strategies

5.1. Trade-offs

These results highlight the importance of collecting data across a broad range of infrared wavelengths, rather than very high spectral or spatial resolution, in order to understand eruption style. For observing Io, low-spatial-resolution data from ground-based telescopes are the only available data for at least the next decade. Although new equipment such as the OSIRIS camera (Laver et al., 2007) provide hyperspectral data over a narrow short-wave infrared wavelength range, we stress that contemporaneous data are needed at a longer wavelength to constrain eruption mode. For ground-based telescopes, the addition of data obtained through the 4.8-μm atmospheric infrared window is ideal for this purpose.

We do not suggest that the quest for higher-spatial-resolution data should not be pursued, just that it should not be at the expense of temporal resolution if those data are obtained at the most useful wavelengths. In the event that a trade-off *has* to be made between spatial, spectral and temporal resolutions, as was often the case with the *Galileo* mission, neither spatial nor spectral resolution are as critical as the breadth of the sampled wavelengths. For terrestrial eruptions, high-spatial-resolution data are vital to locate the position of active vents. However, low-spatial-resolution/high-temporal-resolution data collected (without saturation) at suitable short-wave, mid-, and thermal infrared wavelengths can be used to classify and chart the progression of the eruption.

5.2. Temporal resolution

Thermal emission variability for different eruption styles (e.g., lava fountains, pressurized and persistent lava effusions, lava lakes, and lava dome extrusions) typically follows characteristic temporal trends. For example, whereas activity, expressed as variability in heat loss, waxes and wanes over time scales of days for pressurized lava flow effusions (Harris et al., 2000b), lava fountain events or convective overturn of a lava lake cause short-lived spikes in the radiance time series lasting a few hours (Harris and Neri, 2002; Harris and Thornber, 1999). Thus, for different effusive eruption styles, different temporal scales are appropriate. Regardless of whether activity is taking place on Io or Earth, lava fountains need observations on a time scale of tens of minutes to hours. Channelized flows require (ideally) observations on a time scale of minutes to hours over a period of days because flow rates vary considerably over such time scales (e.g., Bailey et al., 2006). Persistently active lava lakes and domes can be monitored on a weekly or monthly basis for years, but time scales of minutes are required to define and examine cycles of convective overturn at lava lakes (e.g., Flynn et al., 1994; Harris et al., 2005). Likewise, persistent tube-fed flows can be monitored on a daily to weekly basis for years, but time scales of minutes are again required to define short-lived surges in effusion (e.g., Harris and Thornber, 1999).

6. Conclusions

Different effusive eruption styles display characteristic trends in their thermal radiance evolution, as well as in spatial distribution and intensity of radiant heat flux, and therefore can be classified according to their spectral character. As seen by *Galileo* NIMS, for example, different effusive and explosive eruption styles on Io have characteristic "spectral signatures" that can be used for constraining eruption style.

Despite the low spatial resolution of the data currently being acquired of Io's volcanic activity, it is possible to constrain and classify eruption style from the shape of the integrated thermal emission spectrum as well as the ratio of the 2:5-μm thermal emission. This classification is borne out

Table 9
Typical 2:5-μm radiant flux ratios for a sample of volcanoes on Io and Earth.

Volcano	2:5-μm radiant flux ratio	Eruption style
Zal Patera	0.003	Cooled lava flows
Gish Bar Patera	0.006	Cooled lava flows
Lonquimay	*0.027*	*Blocky 'a'a flow*
Loki Patera	0.012 to 0.052	Quiescent lava "sea"
Kilauea 1991	*0.045*	*Insulated flow field*
Kilauea 2000–2001	*0.039 to 0.047*	*Insulated flow field*
Altjirra Patera	0.056	Cooling lava flows
Maui Patera	0.107	Flows or quiescent/inactive lake
Zamama	0.130	Insulated flow field
Amirani	0.148	Insulated flow field
Culann	0.164	Lava flows or lake
Prometheus	0.220	Insulated flow field
Tupan Patera	0.255	Lava lake? Ponded flow? Lava flow?
Monan Patera	0.264	Lava flows?
Pillan	0.725 down to 0.091	Lava fountains, open channel flows
Pele	0.565 to 1.480	Active lava lake
Erebus 2005	*0.573*	*Active lava lake*
Etna 2004	1.08–0.68	Open channel flow
Surt 2001	2.05	Outburst eruption: lava fountains
Loki region 1990	3.48	Outburst: lava fountains and flows

Terrestrial volcanoes are in *italics*.

Table 10
Time scales of volcanic processes.

Time scale	Process
Seconds	Cooling of pyroclasts Cooling of lava surfaces to 1000 K
Hours–days	Lava fountaining
Weeks–months	Open flows
Months–years	Insulated flows
Years-100 s of years	Subsequent cooling of lava flow surfaces (Io) Cooling of shallow intrusions (possible surface detection)
1000 years–10^6 years	Cooling of deep plutons, sensed indirectly through secondary fluids like sulfur on Io and hydrothermal waters on Earth

From: Davies (2007).

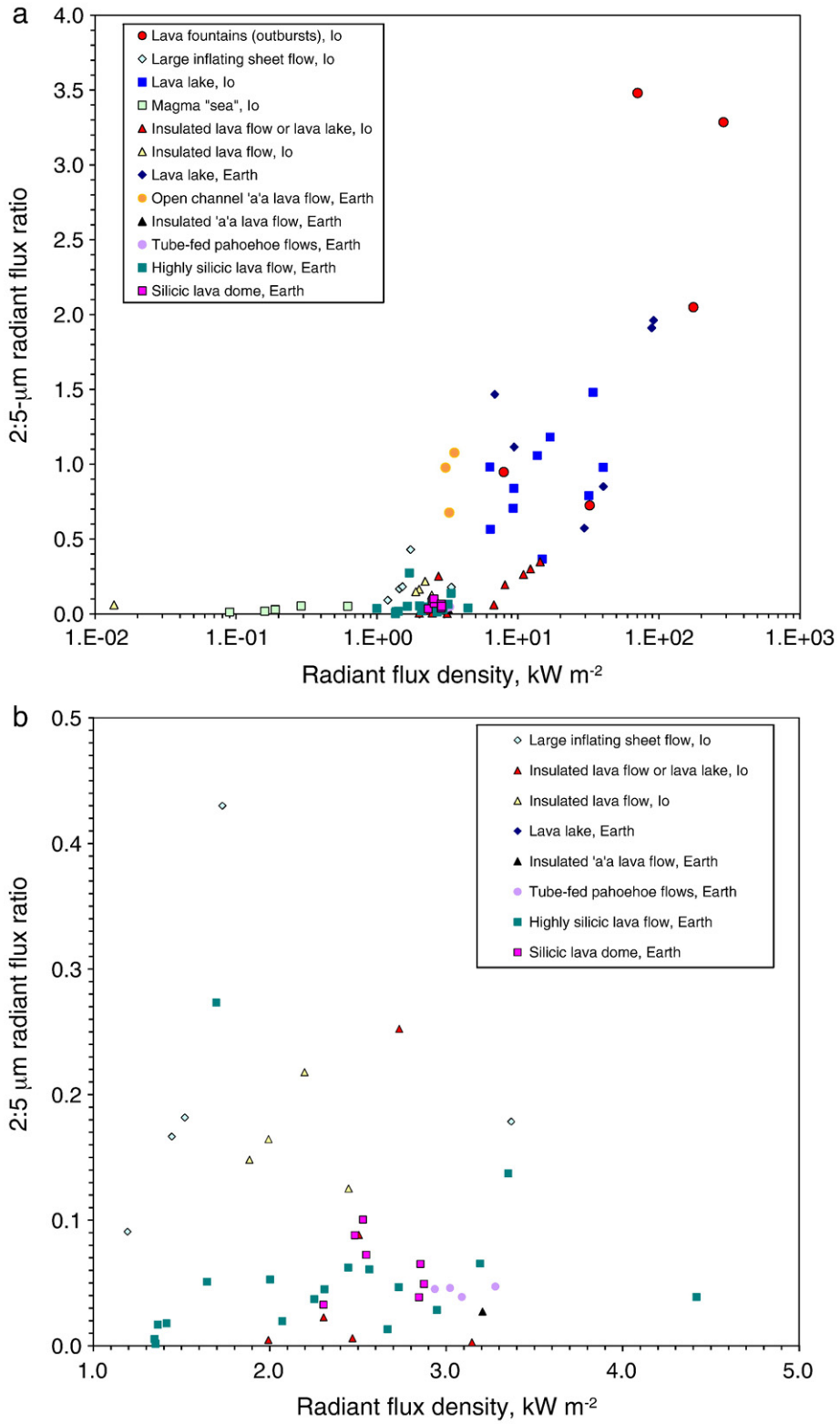

Fig. 13. (a). A plot of radiant flux density against 2:5-μm ratio. High-energy events, such as lava fountains and active lava lakes, are clearly separated from eruptions dominated by the emplacement of insulated flows, or relatively slow emplacement of lava which results in a preponderance of warm (as opposed to hot or incandescent) surfaces. As the hottest area increases in size relative to that of cooler surfaces, radiant flux density increases and the 2:5-μm radiant flux ratio increases. Some data clustering stands out: open channel 'a'a flows (orange circles) have a higher 2:5-μm radiant flux ratio than those seen on terrestrial insulated flows (e.g., lilac circles and green squares) and are clearly separated from a sample of ionian lava flows (yellow triangles), consistent with these ionian flows being pahoehoe-like. The lava fountain data include the Pillan May 1997 datum (see Davies et al., 2001), but not the June 1997 datum, because by that time most thermal emission was probably from large lava flows (Davies et al., 2007). See Fig. 13b for more detail of the insulated flow cases. Loki Patera (light green outlined squares) consistently exhibits a low 2:5-μm radiant flux ratio and radiant flux density that are quite different from any other volcano on Earth or Io. The datum for Altjirra Patera (the yellow triangle in the lower left corner of the plot) is the result of extensive, very cool flows with no significant hot component. Volcanic activity had almost certainly recently ceased at the time of observation in June 1996. (b). Detail of Fig. 13a showing lower-energy eruption styles on Io and Earth. Here, the 2:5-μm radiant flux ratio and radiant flux density are dominated by cool crust that has formed on flows and at domes. See text for caveats regarding the terrestrial data for Kilauea and Lonquimay.

by consideration of similar data for volcanic activity on Earth. We find that data collected at two wavelengths is sufficient if (1) the wavelengths are carefully selected from the 1- to 2-μm and 4- to 5-μm regions, and (2) temporal resolutions are sufficiently high to allow the change in radiant fluxes at these wavelengths to be observed. The measurement of the 2:5-μm ratio is particularly sensitive to changing style of emplacement. For terrestrial data, and when using terrestrial telescopes to image Io, the 4.8-μm window has an atmospheric transmission of better than

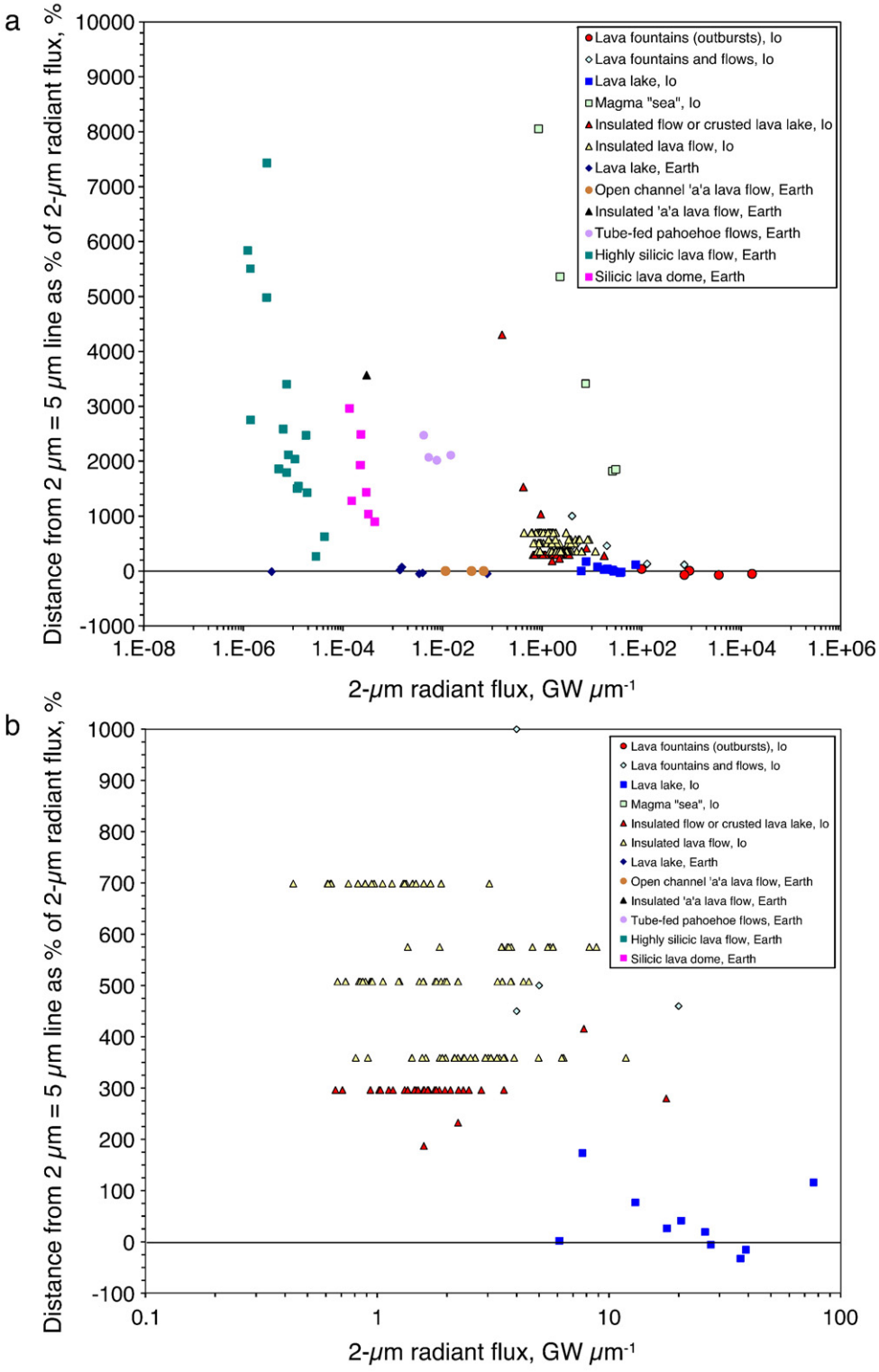

Fig. 14. a). Plot of distance from 2 μm = 5 μm line (see Figs. 10 and 11) for 2-μm radiant flux, presented as a percentage of the 2-μm radiant flux. Two data points for Santiaguito are not shown on this plot (with % values of >10,000%, i.e., very little thermal emission at 2 μm). The most energetic styles of volcanic activity on both Io and Earth (lava fountains and active lava lakes) have in all cases small percentage (<100%) values, or are negative. The relative size of the hottest surface areas to the cool areas controls the position of data along the *y* axis. The absolute size of the hot area, which increases as eruptions become more vigorous, determines position along the *x* axis. The area of the plot for 2-μm thermal emission from 0.1 to 100 GW μm^{-1} is shown in detail in Fig. 14b. b). Detail of the plot of distance from 2 μm = 5 μm line for 2-μm radiant flux, presented as a percentage of the 2-μm radiant flux in Fig. 14a, showing, primarily, insulated flows or crusted lava lakes on Io (red triangles), insulated lava flows on Io (yellow triangles), and lava lakes on Io (blue squares).

70%, and there is little difference between thermal emission at 4.8 μm and 5 μm. Ideally, an observation in the thermal infrared (8–12 μm) would also be obtained to improve constraint on temperature model fits to the data (e.g., Lombardo and Buongiorno, 2006; Oppenheimer et al., 1993a).

Even when an entire volcano is reduced to within one pixel, the thermal signature provides insight into the eruption style. Whereas the most vigorous mafic eruptions (generating the proportionally largest areas at high temperatures) generally do not last longer than a few hours to days, low-effusion-rate activity can persist for years to decades. Table 10 summarizes the typical time scales for different volcanic processes. Observations should ideally be made on time scales an order of magnitude less than the time scale of the phenomenon. A lava fountain, for example, should therefore be imaged on a time scale of minutes.

Fig. 13a shows radiant flux density plotted against the 2:5-μm radiant flux ratio. Fig. 13b shows a detail of the plot for the data including insulated lava flows on both Io and Earth. Fig. 13a and b demonstrates how different classes of eruption exhibit similar characteristics, be they on Earth or Io. For example, active lava lakes generally cluster in the region where the 2:5-μm ratio is 0.5 to 2, and have a high radiant flux density compared to insulated lava flows.

Fig. 14 shows the clustering of eruptions by eruption style as a function of distance from the 2 μm = 5 μm line, as a function of percentage of 2-μm radiant flux. Activity with low or negative percentages (a low value on the *y* axis) indicates a highly vigorous eruption style, such as active lava lakes and lava fountains. A high value on the y axis indicates more thermal emission from the eruption at 5 μm than at 2 μm, as found with eruption styles that create large areas of insulating crust (Santiaguito, Lascar, Popocatepetl, and Loki Patera). A plot like Fig. 14 can be used to constrain eruption style from low-resolution data, so long as wavelength coverage is good.

Fig. 15 summarizes the broad relationships between the composition and viscosity of erupting lava, effusion rate, and style of activity, based on the location of a point determined from data at two wavelengths. This plot could be used to search for silicic flows in future data, on both Earth and Io. Positioning a point on this plot and watching how its location changes with time constrains style of activity.

We now have sufficient data to constrain eruption style using the new Adaptive Optics-enabled multi-wavelength data for Io's volcanism (e.g., Marchis et al., 2005, 2007). These data are now available at spatial resolutions (~160 km per pixel) that are comparable to most of the data obtained by *Galileo* NIMS from orbit around Jupiter. Future 30-m mirror telescopes under construction will improve on this resolution, and the biggest telescopes under study (such as the 100-m-diameter OWL [OverWhelmingly Large] behemoth, under consideration by the European Space Agency) would yield 10-km resolution images of Io.

Our analysis of volcanic spectral signatures is a useful aid in designing the next generation mission to Io (as well as being of use in interpreting data of terrestrial eruptions). One problem with *Galileo* instrument operations, apart from the severe restrictions imposed by the stuck antenna and limited onboard data storage capacity, was that observations of volcanic activity often saturated detectors; it was not possible to know whether a target was going to be active, nor was the widespread distribution of silicate volcanism known before *Galileo* arrived at Jupiter. The modelling of processes and thermal emission (especially high-energy, dynamic processes such as lava fountains and actively overturning lava lakes) will lead to more efficient observation planning and a more versatile instrument capability, with a suggestion for higher (or multiple) gain settings as, for example, on the MODIS sensor.

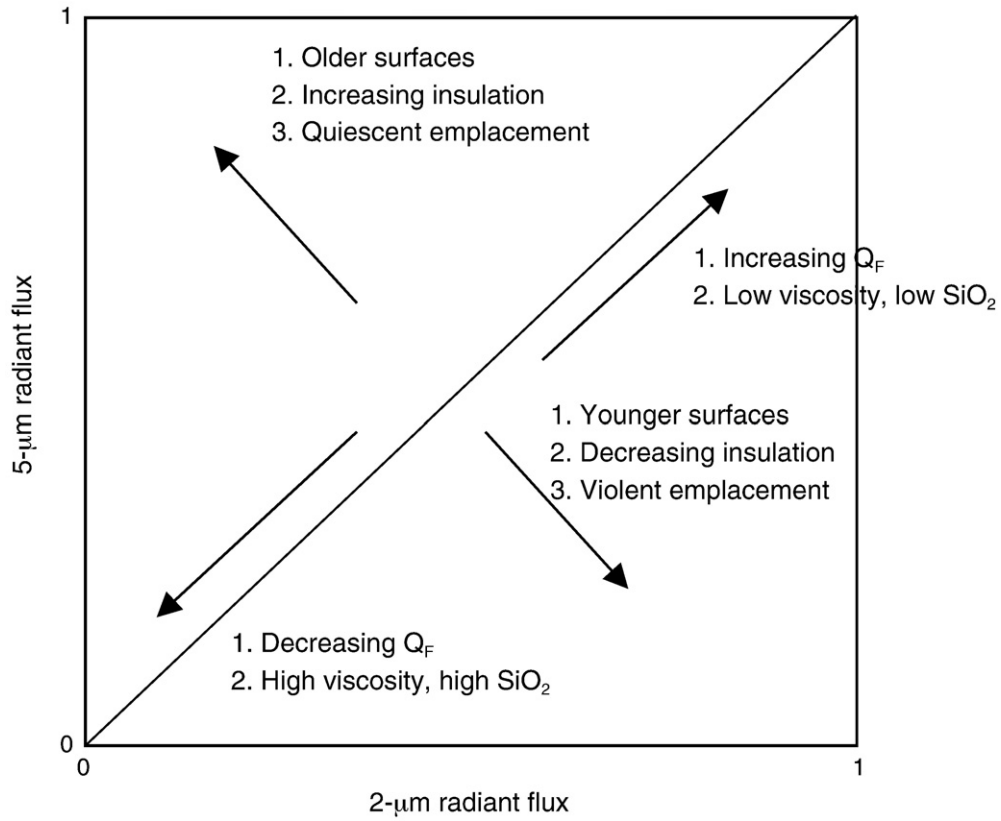

Fig. 15. Variability of eruption style as a function of (a) increasing thermal emission (distance from the origin), (b) degree of lava insulation, and (c) violence of activity (distance from the 2 μm = 5 μm line). The position of a datum on this two-wavelength radiant flux plot (with radiant fluxes determined at 2 μm and 5 μm) is governed by a combination of mutually-controlling factors: eruption style, effusion rate (Q_F) and lava composition.

Lava fountains are expected to be ideal candidates for obtaining data that could be used to constrain lava eruption temperature and magma composition, an important question unanswered after the *Galileo* mission (e.g., Keszthelyi et al., 2007). It would be useful to examine scenarios where lava fountains could be isolated from resulting flows. Imagers on spacecraft could resolve lava fountains on close flybys. *Galileo* managed to do this in 1999 at Tvashtar, although the data were saturated and unusable for constraining eruption temperatures. A high-latitude Io outburst observed in October 1996 (Stansberry et al., 1997) was probably located in a patera, or partially hidden by some other topography. In any case, probably only part of the lava fountain was seen and not the attending flows, as shown by the absence of the expected thermal emission from cooling flows on subsequent nights. Subsequent advances in ground-based observational techniques and telescope design will hopefully provide other high-latitude or near-limb observations of these massive eruptions. Finally, the prospects of future missions to the jovian system are improving. In early 2009, NASA selected Jupiter and Europa as the targets of a new large "flagship" mission, called the *Jupiter Europa Orbiter* (*JEO*) (Clark et al., 2009). The initial mission design includes four close flybys of Io, and opportunities over many years to observe Io from a distance. The ability to identify and track individual volcanic eruptions from a distance based on a few wavelengths of data will greatly increase the return of Io science per returned byte of data. Additionally, a dedicated Io mission, the *Io Volcano Observer* (*IVO*) (McEwen et al., 2009), has been proposed under the auspices of the NASA Discovery program. This analysis, therefore, will greatly aid in designing instrumentation and observations for both of these missions (e.g., Keszthelyi et al., 2009), if the secrets of Io's diverse volcanoes are to be uncovered.

Acknowledgements

Part of this work was carried out at the Jet Propulsion Laboratory—California Institute of Technology, under contract to NASA © 2010. All rights reserved. The authors thank Robert Wright (University of Hawai'i) and David Williams (Arizona State University) for their detailed reviews of the manuscript—this paper was greatly improved as a result. AGD thanks Alison Canning Davies for her meticulous editorial review of the manuscript, and Greg Vaughan for additional comments on the manuscript. AGD is supported by the NASA Outer Planets Research Program Grant WBS344.30.99.05. LPK is supported by NASA Outer Planets Research Program Grant NNH08AI47I.

References

Bailey, J.E., Harris, A.J.L., Dehn, J., Calvari, S., Rowland, S., 2006. The changing morphology of an open lava channel on Mt. Etna. Bulletin of Volcanology 68 (6), 497–515.
Blaney, D.L., Johnson, T.V., Matson, D.L., Veeder, G.J., 1995. Volcanic eruptions on Io: heat flow, resurfacing, and lava composition. Icarus 113, 220–225.
Burgi, P.-Y., Caillet, M., Haefeli, S., 2002. Field temperature measurements at Erta'Ale Lava Lake, Ethiopia. Bulletin of Volcanology 64, 472–485.
Calkins, J., Oppenheimer, C., Kyle, P.R., 2008. Ground-based thermal imaging of lava lakes at Erebus volcano, Antarctica. Journal of Volcanology and Geothermal Research 177 (3), 695–704.
Carlson, R.W., Weissman, P.R., Smythe, W.D., Mahoney, J.C., 1992. Near-Infrared Mapping Spectrometer experiment on *Galileo*. Space Science Reviews 60, 457–502.
Carn, S.A., Oppenheimer, C., 2000. Remote monitoring of Indonesian volcanoes using satellite data from the Internet. International Journal of Remote Sensing 21, 873–910.
Carr, M.H., 1986. Silicate volcanism on Io. Journal of Geophysical Research 91, 3521–3532.
Carter, A.J., Ramsey, M.S., Belousov, A.B., 2007. Detection of a new summit crater on Bezymianny Volcano lava dome: satellite and field-based thermal data. Bulletin of Volcanology 69 (7), 811–815.
Clark, K.B. et al., 2009. Return to Europa: Overview of the Jupiter Europa Orbiter Mission. IEEEAC 2009, paper 1065.
Crisp, J.A., 1984. Rates of magma emplacement and volcanic output. Journal of Volcanology and Geothermal Research 20, 177–211.
Davies, A.G., 1996. Io's volcanism: thermo-physical models of silicate lava compared with observations of thermal emission. Icarus 124, 45–61.
Davies, A.G., 2003a. Temperature, age and crust thickness distributions of Loki Patera on Io from *Galileo* NIMS data: implications for resurfacing mechanism. Geophysical Research Letters 30, 2133–2136.
Davies, A.G., 2003b. Volcanism on Io: estimation of eruption parameters from *Galileo* NIMS data. Journal of Geophysical Research (Planets) 108 (E9), 5106–5120.
Davies, A.G., 2007. Volcanism on Io: A Comparison with Earth. Planetary Science Series, Cambridge University Press, Cambridge. 376pp.
Davies, A.G., 2010. Terrestrial Lava Lake Physical Parameter Estimation Using a Silicate Cooling Model—Implications for a Return to the Volcanic Moon, Io, (Abstract) European Geophysical Union General Assembly, 2–7 May 2010, Austria, Vienna.
Davies, A.G., et al., 1997. Temperature and area constraints of the South Volund Volcano on Io from the NIMS and SSI instruments during the *Galileo* G1 orbit. Geophysical Research Letters 24, 2447.
Davies, A.G., Lopes-Gautier, R., Smythe, W.D., Carlson, R.W., 2000. Silicate cooling model fits to *Galileo* NIMS data of volcanism on Io. Icarus 148, 211–225.
Davies, A.G., et al., 2001. Thermal signature, eruption style, and eruption evolution at Pele and Pillan on Io. Journal of Geophysical Research 106, 33079–33104.
Davies, A.G., Matson, D.L., Veeder, G.J., Johnson, T.V., Blaney, D.L., 2005. Post-solidification cooling and the age of Io's lava flows. Icarus 176, 123–137.
Davies, A.G., et al., 2006a. Monitoring active volcanism with the autonomous sciencecraft experiment on *EO-1*. Remote Sensing of Environment 101 (4), 427–446.
Davies, A.G., et al., 2006b. The heartbeat of the volcano: the discovery of episodic activity at Prometheus on Io. Icarus 184, 460–477.
Davies, A.G., Wilson, L., Keszthelyi, L.P., Williams, D., 2007. Lava flow emplacement at Pillan, Io in 1997: implications for massive basaltic flow emplacement on Earth and Mars. Eos Transactions AGU 88 (52) Fall Meeting Supplement, Abstract P34A-08.
Davies, A.G., et al., 2008a. Multi-instrument remote and *in situ* observations of the Erebus Volcano (Antarctica) Lava Lake in 2005: a comparison with the Pele Lava Lake on the jovian moon Io. Journal of Volcanology and Geothermal Research 177 (3), 705–724.
Davies, A.G., et al., 2008b. Rapid response to volcanic eruptions with an autonomous sensor web: the Nyamulagira eruption of 2006. Proc., IEEE Aerospace Conference, Big Sky, Montana, March 2008.
de Pater, I., et al., 2004. Keck AO observations of Io in and out of eclipse. Icarus 169, 250–263.
Dehn, J., Dean, K.G., Engle, K., Izbekov, P., 2002. Thermal precursors in satellite images of the 1999 eruption of Shishaldin Volcano. Bulletin Of Volcanology 64 (8), 525–534.
Ennis, M.E., Davies, A.G., 2005. Thermal emission variability of Zamama, Culann and Tupan on Io using Galileo Near-Infrared Mapping Spectrometer (NIMS) data. 36th Annual Lunar and Planetary Science Conference, p. 1474.
Flynn, L.P., Mouginis-Mark, P.J., 1995. A comparison of the thermal characteristics of active lava flows and forest fires. Geophysical Research Letters 22, 2577–2580.
Flynn, L.P., Mouginis-Mark, P.J., Gradie, J.C., Lucey, P.G., 1993. Radiative temperature measurements at Kupaianaha lava lake, Kilauea volcano, Hawai'i. Journal Geophysical Research 98, 6461–6476.
Flynn, L.P., Mouginis-Mark, P., Horton, K.A., 1994. Distribution of thermal areas on an active lava flow field. Bulletin of Volcanology 56, 284–296.
Glaze, L.S., Francis, P.W., Rothery, D.A., 1989. Measuring thermal budgets of active volcanoes by satellite remote sensing. Nature 338, 144–146.
Harris, A.J.L., 2008. Modeling lava lake heat loss, rheology, and convection. Geophysical Research Letters 35, L07303. doi:10.1029/2008GL033190.
Harris, A.J.L., Neri, M., 2002. Volumetric observations during paroxysmal eruptions at Mount Etna: pressurized drainage of a shallow chamber or pulsed supply? Journal of Volcanology and Geothermal Research 116 (1–2), 79–95.
Harris, A.J.L., Thornber, C., 1999. Complex effusive events at Kilauea as documented by the GOES satellite and remote video cameras. Bulletin of Volcanology 61 (6), 382–395.
Harris, A.J.L., Vaughan, R.G., Rothery, D.A., 1995. Volcanic detection and monitoring using AVHRR data: the Krafla eruption, 1984. International Journal of Remote Sensing 16, 1001–1020.
Harris, A.J.L., Blake, S., Rothery, D.A., Stevens, N.F., 1997a. A chronology of the 1991 to 1993 Etna eruption using AVHRR data: implications for real time thermal volcano monitoring. Journal Geophysical Research 102, 7985–8003.
Harris, A.J.L., et al., 1997b. Low-cost volcano surveillance from space: case studies from Etna, Krafla, Cerro Negro, Fogo, Lascar and Erebus. Bulletin of Volcanology 59, 49–64.
Harris, A.J.L., et al., 1997c. Chronology of the episode 54 eruption at Kilauea Volcano, Hawaii, from GOES-9 satellite data. Geophysical Research Letters 24, 3281–3284.
Harris, A.J.L., et al., 1998. Calculation of lava effusion rates from Landsat TM data. Bulletin of Volcanology 60, 52–71.
Harris, A.J.L., Wright, R., Flynn, L.P., 1999a. Remote sensing of Mount Erebus Volcano, Antarctica, using polar orbiters: progress and prospects. International Journal of Remote Sensing 20 (15 & 16), 3051–3071.
Harris, A.J.L., Flynn, L.P., Rothery, D.A., Oppenheimer, C., Sherman, S.B., 1999b. Mass flux measurements at active lava lakes: implications for magma recycling. Journal of Geophysical Research-Solid Earth 104 (B4), 7117–7136.
Harris, A.J.L., et al., 2000a. Effusion rate trends at Etna and Krafla and their implications for eruptive mechanisms. Journal of Volcanology and Geothermal Research 102 (3–4), 237–270.
Harris, A.J.L., et al., 2000b. Real-time satellite monitoring of volcanic hot spots. In: Mouginis-Mark, P., Crisp, J.A., Fink, J.H. (Eds.), Remote sensing of active volcanism: AGU Geophysical Monograph, 116, pp. 139–160.
Harris, A.J.L., Flynn, L.P., Matias, O., Rose, W.I., 2002. The thermal stealth flows of Santiaguito dome, Guatemala: implications for the cooling and emplacement of dacitic block-lava flows. Geological Society of America Bulletin 114 (5), 533–546.
Harris, A.J.L., Rose, W.I., Flynn, L.P., 2003. Temporal trends in lava dome extrusion at Santiaguito 1922–2000. Bulletin of Volcanology 65 (2–3), 77–89.

Harris, A.J.L., Flynn, L.P., Matías, O., Rose, W.I., Cornejo, J., 2004. The evolution of an active silicic lava flow field: an ETM+ perspective. Journal of Volcanology and Geothermal Research 135, 147–168.
Harris, A., et al., 2005. Lava effusion rates from hand-held thermal infrared imagery: an example from the June 2003 effusive activity at Stromboli. Bulletin of Volcanology 68 (2), 107–117.
Hom, E.F.Y., et al., 2007. AIDA: an adaptive image deconvolution algorithm application to multi-frame and three-dimensional data. Journal of the Optical Society of America 24 (6), 1580–1600.
Johnson, T.V., Matson, D.L., Brown, R.H., Veeder, G.J., 1986. Infrared emission from Io's volcanoes: evidence for change in a Pele-class source in 1985. Bulletin of the American Astronomical Society 18, 774.
Johnson, T.V., Veeder, G.J., Matson, D.L., Brown, R.H., Nelson, R.M., 1988. Io—evidence for silicate volcanism in 1986. Science 242, 1280–1283.
Keszthelyi, L., McEwen, A., 1997. Thermal models for basaltic volcanism on Io. Geophysical Research Letters 24, 2463.
Keszthelyi, L., et al., 2001. Imaging of volcanic activity on Jupiter's moon Io by *Galileo* during the *Galileo* Europa Mission and the Galileo Millennium Mission. Journal of Geophysical Research 106, 33025–33052.
Keszthelyi, L.P., et al., 2007. New estimates for Io eruption temperatures: implications for the interior. Icarus 192, 491–502.
Keszthelyi, L.P., Davies, A.G., McEwen, A.S., 2009. Optimal wavelengths for studying thermal emission from active volcanoes on Io. Lunar and Plan. Sci. Conf. XL.
Laver, C., Pater, I.D., Marchis, F., 2007. Tvashtar awakening detected in April 2006 with OSIRIS at the W.M. Keck Observatory. Icarus 191 (2), 749–754.
Leone, G., et al., 2009. Volcanic history, geologic analysis and map of the Prometheus Patera region on Io. Icarus 187, 93–105.
Lombardo, V., Buongiorno, M.F., 2006. Lava flow thermal analysis using three infrared bands of remote-sensing imagery: a study case from Mount Etna 2001 eruption. Remote Sensing of Environment 101 (2), 141–149.
Lopes, R.M.C., et al., 2001. Io in the near infrared: Near-Infrared Mapping Spectrometer (NIMS) results from the *Galileo* flybys in 1999 and 2000. Journal of Geophysical Research 106, 33053–33078.
Lopes, R.M.C., et al., 2004. Lava lakes on Io: observations of Io's volcanic activity from *Galileo* NIMS during the 2001 fly-bys. Icarus 169 (1), 140–174.
Lopes-Gautier, R., et al., 1997. Hot spots on Io: initial results from *Galileo*'s near infrared mapping spectrometer. Geophysical Research Letters 24, 2439.
Lopes-Gautier, R., et al., 1999. Active volcanism on Io: global distribution and variations in activity. Icarus 140, 243–264.
Marchis, F., Prangé, R., Fusco, T., 2001. A survey of Io's volcanism by adaptive optics observations in the 3.8-um thermal band (1996–1999). Journal of Geophysical Research 106, 33141–33160.
Marchis, F., et al., 2002. High-resolution Keck adaptive optics imaging of violent volcanic activity on Io. Icarus 160, 124–131.
Marchis, F., et al., 2005. Keck AO survey of Io global volcanic activity between 2 and 5 microns. Icarus 176, 96–122.
Marchis, F., Spencer, J.R., Lopes, R.M.C., Davies, A.G., Dumas, C., 2007. Monitoring Io volcanism with AO telescopes during and after the NH flyby. Eos Transactions AGU 88 (52) Fall Meeting Supplement, Abstract P53C-08.
Matson, D.L., et al., 2006. Io: Loki Patera as a magma sea. Journal of Geophysical Research (Planets) 111 (E09002). doi:10.1029/2006JE002703.
McEwen, A.S., et al., 1997. High-temperature hot spots on Io as seen by the *Galileo* solid state imaging (SSI) experiment. Geophysical Research Letters 24, 2443.
McEwen, A.S., et al., 1998a. Active volcanism on Io as seen by *Galileo* SSI. Icarus 135, 181–219.
McEwen, A.S., et al., 1998b. High-temperature silicate volcanism on Jupiter's moon Io. Science 281, 87–90.
McEwen, A.S., et al., 2000. *Galileo* at Io: results from high-resolution imaging. Science 288, 1193–1198.
McEwen, A. et al., 2009. *Io Volcano Observer* (*IVO*), 40th Lunar and Planetary Science Conference, abstract 1876, on CD-ROM.
Milazzo, M.P., et al., 2005. Volcanic activity at Tvashtar Catena, Io. Icarus 179, 235–251.
Morabito, L.A., Synnott, S.P., Kupferman, P.N., Collins, S.A., 1979. Discovery of currently active extraterrestrial volcanism. Science 204, 972.
Oppenheimer, C., 1991. Lava flow cooling estimated from *Landsat* Thematic Mapper Infrared Data—the Lonquimay eruption (Chile, 1989). Journal of Geophysical Research-Solid Earth 96 (B13), 21865–21878.
Oppenheimer, C., Yirgu, G., 2002. Thermal imaging of an active lava lake: Erta 'Ale volcano, Ethiopia. International Journal of Remote Sensing 23 (22), 4777–4782.
Oppenheimer, C., Rothery, D.A., Pieri, D.C., Abrams, M.J., Carrere, V., 1993a. Analysis of Airborne Visible Infrared Imaging Spectrometer (AVIRIS) data of volcanic hot-spots. International Journal of Remote Sensing 14 (16), 2919–2934.
Oppenheimer, C., Francis, P.W., Rothery, D.A., Carlton, R.W.T., Glaze, L.S., 1993b. Infrared image-analysis of volcanic thermal features—Lascar Volcano, Chile, 1984–1992. Journal of Geophysical Research-Solid Earth 98 (B3), 4269–4286.
Patrick, M.R., et al., 2005. First recorded eruption of Mount Belinda volcano (Montagu Island), South Sandwich Islands. Bulletin Of Volcanology 67 (5), 415–422.
Pearl, J., Sinton, W.M., 1982. Hot spots of Io. In: Morrison, D. (Ed.), Satellites of Jupiter. University of Arizona Press, Tucson, pp. 724–755.
Radebaugh, J., et al., 2004. Observations and temperatures of Io's Pele Patera from *Cassini* and *Galileo* spacecraft images. Icarus 169, 65–79.
Rathbun, J.A., Spencer, J.R., Davies, A.G., Howell, R.R., Wilson, L., 2002. Loki, Io: a periodic volcano. Geophysical Research Letters 29, 84-1.
Rothery, D.A., Francis, P.W., Wood, C.A., 1988. Volcano monitoring using short wavelength infrared data from satellites. Journal Geophysical Research 93, 7993–8008.
Rothery, D.A., Coppola, D., Saunders, C., 2005. Analysis of volcanic activity patterns using MODIS thermal alerts. Bulletin of Volcanology 67 (6), 539–556.
Sagan, C., 1979. Sulphur flows on Io. Nature 280, 750–753.
Simkin, T., Siebert, L., 1994. Volcanoes of the World, 2nd ed. Geoscience Press in association with the Smithsonian Institution Global Volcanism Program, Tucson, AZ.
Smythe, W.D., et al., 1995. Galilean satellite observation plans for the near-infrared mapping spectrometer experiment on the *Galileo* spacecraft. Journal of Geophysical Research 100, 18957–18972.
Spampinato, L., Oppenheimer, C., Calvari, S., Cannata, A., Montalto, P., 2008. Lava lake surface characterization by thermal imaging: Erta 'Ale volcano (Ethiopia). Geochemistry, Geophysics, and Geosystems 9 (12), Q12008. doi:10.1029/2008GC002164.
Spencer, J.R., Schneider, N.M., 1996. Io on the Eve of the *Galileo* Mission. Annual Review of Earth and Planetary Sciences 24, 125–190.
Spencer, J.R., et al., 2007. Io volcanism seen by new horizons: a major eruption of the Tvashtar Volcano. Science 318 (5848), 240–243.
Stansberry, J.A., Spencer, J.R., Howell, R.R., Dumas, C., Vakil, D., 1997. Violent silicate volcanism on Io in 1996. Geophysical Research Letters 24, 2455.
Sutton, A.J., Elias, T., Kauahikaua, J., 2003. Lava-effusion rates for the Pu'u 'O'o-Kupaianaha eruption derived from SO_2 emissions and very low frequency (VLF) measurements. U.S. Geological Survey Professional Paper 1676, 137–148.
Turtle, E.P., et al., 2004. The final *Galileo* SSI observations of Io: orbits G28-I33. Icarus 169, 3–28.
Vaughan, R.G., Hook, S.J., Ramsey, M.S., Realmuto, V.J., Schneider, D.J., 2005. Monitoring eruptive activity at Mount St. Helens with TIR image data. Geophysical Research Letters 32 (19), L19305.
Veeder, G.J., Matson, D.L., Johnson, T.V., Blaney, D.L., Goguen, J.D., 1994. Io's heat flow from infrared radiometry: 1983–1993. Journal of Geophysical Research 99, 17095–17162.
Veeder, G., Davies, A.G., Garbeil, H., Matson, D.L., Johnson, T.V., 2009. Dark Flow Fields on Io. Icarus 204, 239–253.
Williams, D.A., Davies, A.G., Keszthelyi, L.P., Greeley, R., 2001a. The summer 1997 eruption at Pillan Patera on Io: implications for ultrabasic lava flow emplacement. Journal of Geophysical Research-Planets 106, 33105–33120.
Williams, D.A., Greeley, R., Lopes, R.M.C., Davies, A.G., 2001b. Evaluation of sulfur flow emplacement on Io from *Galileo* data and numerical modeling. Journal Of Geophysical Research-Planets 106 (E12), 33161–33174.
Wilson, L., Head, J.W., 1981. Ascent and eruption of basaltic magma on the Earth and Moon. Journal of Geophysical Research 86, 2971–3001.
Wooster, M.J., Rothery, D.A., 1997a. Thermal monitoring of Lascar Volcano, Chile, using infrared data from the Along Track Scanning Radiometer: a 1992–1995 time-series. Bulletin of Volcanology 58, 566–579.
Wooster, M.J., Rothery, D.A., 1997b. Time-series analysis of effusive volcanic activity using the *ERS* Along Track Scanning Radiometer: the 1995 eruption of Fernandina volcano, Galapagos Islands. Remote Sensing of Environment 62, 109–117.
Wright, R., Flynn, L.P., 2003. On the retrieval of lava flow surface temperatures from infrared satellite data. Geology 31, 893–896.
Wright, R., Pilger, E., 2008. Satellite observations reveal little inter-annual variability in the radient flux from the Mount Erebus lava lake. Journal of Volcanology and Geothermal Research 177, 687–694.
Wright, R., Flynn, L.P., Harris, A.J.L., 2001. Evolution of lava flow-fields at Mount Etna, 27–28 October 1999, observed by *Landsat 7* ETM+. Bulletin of Volcanology 63 (1), 1–7.
Wright, R., Flynn, L.P., Garbeil, H., Harris, A.J.L., Pilger, E., 2004. MODVOLC: near-real-time thermal monitoring of global volcanism. Journal of Volcanology and Geothermal Research 135 (1–2), 29–49.
Wright, R., Garbeil, H., Davies, A.G., 2010. The cooling rate of some active lavas determined using an orbital imaging spectrometer. Journal of Geophysical Research 115, B06205.